Tuning and performance comparison of multiresonant piezoelectric shunts

Journal Title
XX(X):1–20

DOI: 10.1177/ToBeAssigned
www.sagepub.com/
SAGE

Ghislain Raze[1], Jennifer Dietrich[1] and Gaetan Kerschen[1]

Abstract

This work presents tuning rules for piezoelectric shunts aiming to mitigate multiple structural resonances. Starting from a specification procedure of the shunt characteristics, the electrical parameters are derived for shunt topologies proposed in the literature, namely Hollkamp's shunt, the current flowing shunt, the series parallel impedance structure and the current blocking shunt. Effective vibration mitigation of multiple structural modes is demonstrated numerically and experimentally on a piezoelectric beam. Performance in terms of vibration reduction obtained with the different shunts is shown to be comparable if similar shunt characteristics are considered.

Keywords

Piezoelectric shunt, Multimodal damping, Current flowing, Current blocking, Series-parallel impedance

Introduction

Piezoelectric shunt damping is a damping enhancement technique exploiting the transduction capability of piezoelectric materials to mitigate the vibrations of a host structure. A piezoelectric material is able to convert a part of its mechanical energy into electrical energy which can be dissipated by properly-tuned shunts, resulting in effective damping in the controlled structure. Resistive shunts or resonant shunts with series (Hagood and von Flotow 1991) or parallel (Wu 1996) RL elements are classically used to mitigate a single resonant mode.

Vibration damping of multiple modes may be achieved with multiple transducers by individually shunting each transducer with classical RL shunts (Toftekær and Høgsberg 2020). These transducers may alternatively be interconnected by an electrical network, see, e.g., Darleux et al. (2020). Multimodal control is also achievable with a single piezoelectric transducer. A first approach consists in using a mere resistive shunt, which is broadband in nature. The vibration attenuation exhibited by this approach is however often limited, and approaches were proposed to enhance its performance with a negative capacitance (Berardengo et al. 2016) or with a non-resonant inductor (Berardengo et al. 2021). A second approach consists in using shunts that resonate with the piezoelectric transducer at multiple frequencies (Moheimani and Fleming 2006). This latter approach is adopted in this work.

Several circuit topologies were proposed to achieve multimodal resonant damping with a single transducer. Edberg et al. (1991) added a second branch to a classical series RL shunt to mitigate two resonances, and this circuit was later generalized to an arbitrary number of modes by Hollkamp (1994). A number of other topologies were proposed since then, such as the current blocking shunt (Wu 1998; Agneni et al. 2006), the current flowing shunt (Behrens et al. 2003), the series-parallel impedance structure (Fleming et al. 2003) and a Cauer-type network (Goldstein 2011). Each of these circuits proved rather difficult to tune, and numerical optimization was often needed for circuits with known (Fleming et al. 2002; Cigada et al. 2012; Gardonio et al. 2019) or unknown (Berardengo et al. 2017; Dal Bo et al. 2022) topology. The latter approach either requires a further step to synthesize the circuit afterwards or requires the analysis of multiple architectures, but has the potential advantage of allowing for more optimal solutions than the former since it is less restrictive. A sequential tuning procedure based on effective characteristics associated with electrical resonances was recently proposed by Raze et al. (2020) for the current blocking shunt, but this procedure is limited to a particular shunt topology, does not provide a quantitative insight into the arbitrary choices made beforehand, and relies on an ad hoc identification procedure which may fail for structures with, e.g., closely-spaced modes. Finally, we note that there exists few objective comparisons between these different topologies (see, e.g., Berardengo et al. (2017)), making it difficult to distinguish between the strengths and weaknesses of each type of circuit.

Raze et al. (2021) recently proposed a model-less sequential specification procedure for a generic shunt. This shunt was emulated by a digital vibration absorber, making it unnecessary to determine its topology. To progress toward the fully passive implementation of such circuits, this work proposes to exploit this specification methodology to tune various shunts whose topology has previously been introduced in the literature. The proposed approach

[1]University of Liège, Liège, Belgium

Corresponding author:
Ghislain Raze
Space Structures and Systems Laboratory (S3L), Department of Aerospace and Mechanical Engineering, University of Liège
Quartier Polytech 1 (B52/3)
Allée de la Découverte 9
Liège, B-4000, Belgium
Email: g.raze@uliege.be

allows the designer to make an informed decision on the control authority on each targeted mode, and to achieve effective multimodal vibration damping with either topology. Additionally, performance in terms of vibration mitigation is assessed for the different topologies, and it is shown that they are all equivalent provided that the required authority on each controlled mode is identical.

This article is organized as follows. The principles of the specification procedure for shunt circuits are first briefly recalled. The tuning of the electrical parameters is then addressed for different circuit topologies, namely Hollkamp's shunt, the current flowing shunt, the series parallel impedance structure and the current blocking shunt. Numerical verification and experimental validation of the proposed approach are eventually carried out on a piezoelectric beam.

Specification procedure for the shunt

The specification procedure proposed by Raze et al. (2021) forms the starting point of this paper, and is summarized in this section. A piezoelectric transducer may be modeled as a current source in parallel with a capacitor of capacitance C_p^ε. This capacitance corresponds to the capacitance at constant strain (or blocked capacitance) of the transducer. It can be shown that Norton's equivalent admittance of the parallel connection of the piezoelectric capacitance with a generic lossless shunt of admittance Y_s,

$$Y_N(s) = sC_p^\varepsilon + Y_s(s), \tag{1}$$

takes the specific form

$$\frac{s}{Y_N(s)} = \frac{1}{C_p^\varepsilon}\left(r_0 + \sum_{i=1}^{N_s} \frac{r_i s^2}{s^2 + z_i^2}\right), \tag{2}$$

where s is Laplace's variable, z_i is a zero of Norton's admittance and r_i its associated residue. This admittance plays the role of a feedback controller acting to damp the vibrations of the host structure. Alternatively, when the piezoelectric transducer is electrically modeled as a voltage source in series with a capacitor of capacitance C_p^ε, Thévenin's impedance of a series connection with the shunt of impedance $Z_s = Y_s^{-1}$,

$$Z_T(s) = \frac{1}{sC_p^\varepsilon} + Z_s(s), \tag{3}$$

has the specific form

$$\frac{1}{sZ_T(s)} = C_p^\varepsilon\left(r_0 + \sum_{i=1}^{N_s} \frac{r_i}{\dfrac{s^2}{z_i^2} + 1}\right), \tag{4}$$

and can also be interpreted as a feedback controller acting on the host structure. Furthermore, it can be shown that Norton's admittance and Thévenin's impedance have the same zeros and residues (except for r_0). Equations (2) and (4) both contain a sum of terms representing electrical resonances of the circuit at frequencies z_i. The associated residues r_i may be seen as resonant amplitudes. It was demonstrated that they determine the *effective* modal electromechanical coupling factor (MEMCF) $\widehat{K}_{c,r}$ of the *circuit* with mode r to the MEMCF $K_{c,r}$ of the *transducer* as

$$\widehat{K}^2_{c,r(k)} \approx r_k K^2_{c,r(k)}. \tag{5}$$

From Equation (5), it is desirable from a control performance viewpoint to have residues as high as possible in order to maximize the effective MEMCF, because the greater the MEMCF, the greater the vibration attenuation on the targeted mode (Thomas et al. 2012). However, these residues are constrained by passivity requirements on the shunt, which mathematically translates into

$$r_i \geq 0, \qquad \sum_{i=0}^{N_s} r_i \leq 1, \tag{6}$$

highlighting the performance limits of passive shunts targeting multiple structural modes. Indeed, Equation (6) implies that $r_i \leq 1$, and thus by Equation (5) the MEMCF of the circuit cannot be greater than that of the transducer. If multiple modes are controlled, the sum implies that control performance has to be traded-off between them.

Raze et al. (2021) proposed a specification procedure taking as input the piezoelectric capacitance at constant strain as well as the short- and open-circuit resonance frequencies of the structure, and a set of targeted modes with associated residues representing the desired control authority. The output of the method is a set of electrical resonance frequencies z_i and associated modal damping ratios ζ_i, defining either Norton's dissipative admittance

$$Y_{N,d}(s) = sC_p^\varepsilon\left(r_0 + \sum_{i=1}^{N_s} \frac{r_i s^2}{s^2 + 2\zeta_i z_i s + z_i^2}\right)^{-1}, \tag{7}$$

or Thévenin's dissipative impedance

$$Z_{T,d}(s) = \frac{1}{sC_p^\varepsilon}\left(r_0 + \sum_{i=1}^{N_s} \frac{r_i}{\dfrac{s^2}{z_i^2} + 2\zeta_i\dfrac{s}{z_i} + 1}\right)^{-1}. \tag{8}$$

The tuning parameters z_i and ζ_i are determined using formulae from a single-degree-of-freedom *baseline case* which can be either the series RL shunt or parallel RL shunt.

Equations (2) and (4) represent exactly the behavior of the lossless counterparts of passive shunts of known topology which have been proposed in the literature, namely Hollkamp's shunt, the current flowing (CF) shunt, the series-parallel impedance structure (SPIS) and the current blocking (CB) shunt. This article leverages the specification methodology proposed by Raze et al. (2021) to tune these circuits. The tuning procedure starts by considering the lossless circuits (containing only capacitors and inductors) and tuning them using Equation (2) or (4). Equation (7) or (8) can then be used to tune the resistances of these shunts to optimally mitigate the targeted structural resonances. The specificities of the tuning procedure depend on the considered topology and are detailed in the sequel.

Hollkamp's and current flowing shunt circuits tuning

Two multimodal shunts proposed by Hollkamp (1994) and Behrens et al. (2003) are featured in Figure 1. The lossless

circuits ($R_i = 0$) connected in parallel to a capacitor are shown in Figure 2 and are used to build Norton's equivalent admittance Y_N. It can be recognized that the resulting circuits are equivalent to Foster's first canonical form (Chen 2018).

Tuning either type of circuit requires to compute the zero-pole-gain (ZPK) representation of Y_N. From Equation (2),

$$Y_N(s) = sC_p^\varepsilon \left(r_0 + \sum_{i=1}^{N_s} \frac{r_i s^2}{s^2 + z_i^2} \right)^{-1} = Ks \frac{\prod_{i=1}^{N_s}(s^2 + z_i^2)}{\prod_{i=1}^{N_s}(s^2 + p_i^2)}. \quad (9)$$

The zeros z_i of Norton's equivalent admittance are known from the specification procedure, and its poles p_i can be found as the solution of the polynomial equation

$$r_0 \prod_{i=1}^{N_s}(s^2 + z_i^2) + \sum_{i=1}^{N_s} r_i s^2 \prod_{k=1,k\neq i}^{N_s} (s^2 + z_k^2) = 0. \quad (10)$$

Realistically, this polynomial is of moderate order. Moreover, its coefficients are known. Thus, the poles can readily be found with a computer. We note that when $r_0 = 0$, $p_1 = 0$ is a solution and thus Y_N has a simple pole at $s = 0$, whereas it has a simple zero at $s = 0$ if $r_0 \neq 0$. The gain K can be determined later.

Hollkamp's shunt circuit

The admittance of the lossless circuit featured in Figure 2a reads

$$Y_N(s) = sC_p^\varepsilon + \frac{1}{sL_0} + \sum_{n=1}^{N_s-1} \frac{\frac{1}{L_n}s}{s^2 + \frac{1}{L_nC_n}} = \frac{K}{s} \frac{\prod_{i=1}^{N_s}(s^2 + z_i^2)}{\prod_{i=1}^{N_s-1}(s^2 + p_i^2)} \quad (11)$$

In this equation, the admittance computed as the parallel connection of a capacitor, an inductor and $N_s - 1$ branches of series LC circuits is represented in its partial fraction expansion. The fact that there is a simple pole at $s = 0$ indicates that this circuit can only be used if $r_0 = 0$. Equating the admittance to its ZPK representation and taking the limit for $s \to \infty$ in Equation (11), the gain K is found to be

$$K = C_p^\varepsilon, \quad (12)$$

which completely specifies the ZPK representation. The electrical parameters may then be derived from it. The admittance possesses several poles which can directly be related to the electrical parameters by

$$p_n = \frac{1}{\sqrt{L_nC_n}}, \quad (13)$$

and the inductances can be evaluated with the the cover-up method (Franklin et al. 2015). This gives the single inductance L_0 as

$$L_0 = \lim_{s\to 0} sY_N(s) = \frac{1}{C_p^\varepsilon} \frac{\prod_{i=1}^{N_s-1} p_i^2}{\prod_{i=1}^{N_s} z_i^2} \quad (14)$$

whereas the inductances in the LC branches are identified as

$$L_k = \frac{1}{2} \lim_{s\to \pm jp_k} (s \mp jp_k) Y_N(s) = -\frac{p_k^2}{C_p^\varepsilon} \frac{\prod_{i=1,i\neq k}^{N_s-1}(p_i^2 - p_k^2)}{\prod_{i=1}^{N_s}(z_i^2 - p_k^2)}, \quad (15)$$

where j is the unit imaginary number. Finally, the capacitances are determined from Equation (13) as

$$C_k = \frac{1}{L_k p_k^2}. \quad (16)$$

Current flowing shunt circuit

The admittance of the undamped CF shunt shown in Figure 2b reads

$$Y_N(s) = sC_p^\varepsilon + \sum_{n=1}^{N_s} \frac{\frac{1}{L_n}s}{s^2 + \frac{1}{L_nC_n}} = Ks \frac{\prod_{i=1}^{N_s}(s^2 + z_i^2)}{\prod_{i=1}^{N_s}(s^2 + p_i^2)}. \quad (17)$$

This time, the simple zero at $s = 0$ imposes $r_0 \neq 0$. In a similar way to Hollkamp's shunt, the gain K is found to be

$$K = C_p^\varepsilon, \quad (18)$$

whereas the inductances are given by

$$L_k = \frac{1}{C_p^\varepsilon} \frac{\prod_{i=1,i\neq k}^{N_s}(p_i^2 - p_k^2)}{\prod_{i=1}^{N_s}(z_i^2 - p_k^2)}, \quad (19)$$

and the capacitances by

$$C_k = \frac{1}{L_k p_k^2}. \quad (20)$$

It can be noted that when $r_0 \to 0$, one of the double roots of Equation (10), say, p_1, tends to zero. Then, Equation (20) shows that $C_1 \to \infty$, i.e., the capacitance becomes nearly equivalent to a short-circuit. By replacing C_1 in Figure 1b by a short-circuit, the same circuit topology as that of Hollkamp's shunt is obtained. Therefore, the CF shunt tends to Hollkamp's shunt as $r_0 \to 0$.

Resistances tuning

In the case of Hollkamp's and the CF shunts, the best baseline case to use in the specification procedure (Raze et al. 2021) is the series RL shunt. A heuristic justification is that the resistors are placed in series with the inductors in these circuits (and in particular when $N_s = 1$, Hollkamp's shunt reduces to a series RL shunt). Tuning based on the parallel RL circuit can also be used but was observed to give less optimal results.

The purpose of the following procedure is to impose approximately the desired modal damping on the zeros of Thévenin's impedance. From Equation (3), its inverse is

$$\frac{1}{Z_{T,d}(s)} = \frac{1}{\frac{1}{sC_p^\varepsilon} + \frac{1}{Y_s(s)}} = Y_s(s) - \frac{1}{sC_p^\varepsilon} \frac{Y_s^2(s)}{1 + \frac{Y_s(s)}{sC_p^\varepsilon}}, \quad (21)$$

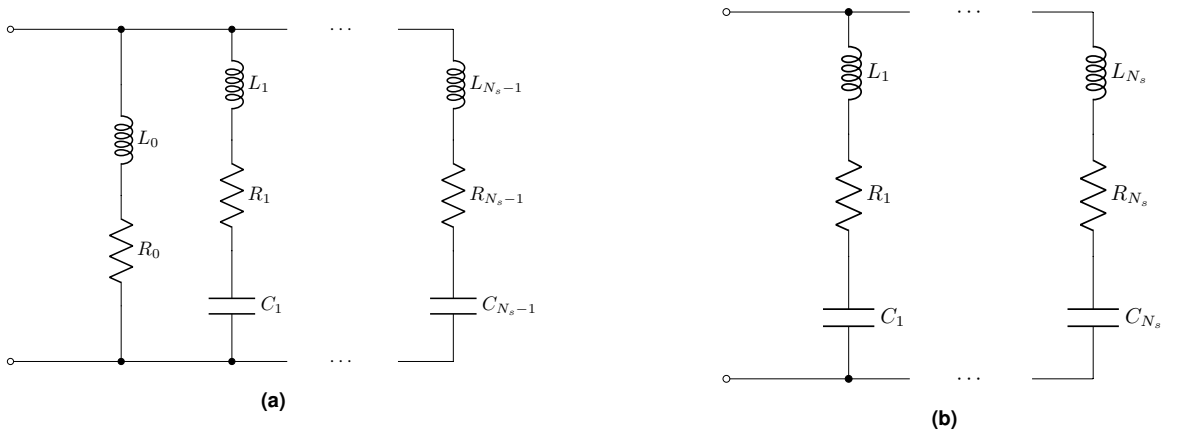

Figure 1. Hollkamp's shunt (a) and current flowing shunt (b).

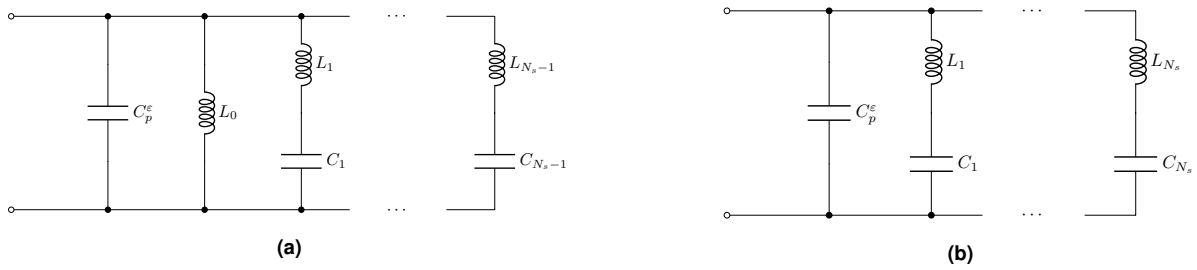

Figure 2. Norton's admittance model of a piezoelectric transducer connected to Hollkamp's losless shunt (a) and a lossless current flowing shunt (b).

where Hollkamp's dissipative shunt admittance is given by

$$Y_s(s) = \frac{1}{sL_0 + R_0} + \sum_{n=1}^{N_s-1} \frac{s}{L_n s^2 + R_n s + \frac{1}{C_n}} \tag{22}$$

and can also be expressed by

$$Y_s(s) = s\mathbf{1}_{1\times N_s} \left(\mathbf{E}_H + s\mathbf{R}_H + s^2\mathbf{L}_H\right)^{-1} \mathbf{1}_{N_s\times 1}, \tag{23}$$

where

$$\mathbf{E}_H = \mathbf{diag}\begin{bmatrix}0 & C_1^{-1} & \cdots & C_{N_s-1}^{-1}\end{bmatrix}, \tag{24}$$

$$\mathbf{R}_H = \mathbf{diag}\begin{bmatrix}R_0 & R_1 & \cdots & R_{N_s-1}\end{bmatrix} \tag{25}$$

and

$$\mathbf{L}_H = \mathbf{diag}\begin{bmatrix}L_0 & L_1 & \cdots & L_{N_s-1}\end{bmatrix} \tag{26}$$

are elastance, resistance and inductance matrices, respectively, $\mathbf{1}_{m\times n}$ is a $m \times n$ is a matrix whose entries are all equal to one, and **diag** denotes a diagonal matrix. Using this matrix-based model and by comparing Equation (21) with the Sherman-Morrison formula (Equation (95)), the inverse of Thévenin's impedance given in Equation (21) can be obtained if the inverted matrix is rank-one updated, i.e.,

$$\frac{1}{Z_{T,d}(s)} = s\mathbf{1}_{1\times N_s}\Bigg(\mathbf{E}_H + \frac{1}{C_p^\varepsilon}\mathbf{1}_{N_s\times 1}\mathbf{1}_{1\times N_s} + s\mathbf{R}_H + s^2\mathbf{L}_H\Bigg)^{-1}\mathbf{1}_{N_s\times 1}. \tag{27}$$

In the lossless case, the zeros of Thévenin's impedance are the generalized eigenvalues of the generalized eigenvalue problem

$$\left(\mathbf{E}_H + \frac{1}{C_p^\varepsilon}\mathbf{1}_{N_s\times 1}\mathbf{1}_{1\times N_s}\right)\mathbf{\Phi}_e = \mathbf{L}_H\mathbf{\Phi}_e\mathbf{\Omega}_e^2, \tag{28}$$

where

$$\mathbf{\Omega}_e = \mathbf{diag}\begin{bmatrix}z_1 & \cdots & z_{N_s}\end{bmatrix}, \tag{29}$$

and $\mathbf{\Phi}_e$ can be seen as an electrical mode shape matrix. In order to impose the desired damping on the zeros of Thévenin's impedance, the mode shape matrix should ideally diagonalize the resistance matrix. However, this is not the case in general because the electrical resonances do not localize to a single branch (which would result in a diagonal matrix $\mathbf{\Phi}_e$) but are distributed over the whole circuit, and the following relation is only approximate

$$\mathbf{\Phi}_e^T\mathbf{R}_H\mathbf{\Phi}_e \approx 2\mathbf{Z}_e\mathbf{\Omega}_e, \tag{30}$$

where

$$\mathbf{Z}_e = \mathbf{diag}\begin{bmatrix}\zeta_1 & \cdots & \zeta_{N_s}\end{bmatrix}. \tag{31}$$

By enforcing this relation on the diagonal of this resulting matrix (regardless of its off-diagonal elements), the following set of resistances can be obtained:

$$\begin{bmatrix}R_0\\ \vdots \\ R_{N_s-1}\end{bmatrix} = \begin{bmatrix}\phi_{e,0,1}^2 & \cdots & \phi_{e,(N_s-1),1}^2\\ \vdots & \ddots & \vdots \\ \phi_{e,0,N_s}^2 & \cdots & \phi_{e,(N_s-1),N_s}^2\end{bmatrix}^{-1}\begin{bmatrix}2\zeta_1 z_1\\ \vdots \\ 2\zeta_{N_s} z_{N_s}\end{bmatrix}. \tag{32}$$

The same procedure can be followed for the CF shunt by simple adaptation of the involved matrices, since its

dissipative admittance is given by

$$Y_s(s) = \sum_{n=1}^{N_s} \frac{s}{L_n s^2 + R_n s + \frac{1}{C_n}}, \tag{33}$$

or, equivalently,

$$Y_s(s) = s\mathbf{1}_{1\times N_s} \left(\mathbf{E}_{CF} + s\mathbf{R}_{CF} + s^2\mathbf{L}_{CF}\right)^{-1} \mathbf{1}_{N_s\times 1}. \tag{34}$$

in which

$$\mathbf{E}_{CF} = \mathbf{diag}\begin{bmatrix} C_1^{-1} & \cdots & C_{N_s}^{-1} \end{bmatrix}, \tag{35}$$

$$\mathbf{R}_{CF} = \mathbf{diag}\begin{bmatrix} R_1 & \cdots & R_{N_s} \end{bmatrix} \tag{36}$$

and

$$\mathbf{L}_{CF} = \mathbf{diag}\begin{bmatrix} L_1 & \cdots & L_{N_s} \end{bmatrix}. \tag{37}$$

Summary

The proposed tuning procedure for Hollkamp's and the CF shunts goes as follows. Starting from a set of targeted modes and associated residues r_i,

1. Compute each frequency z_i and damping ratio ζ_i with the series RL baseline from the approach proposed by Raze et al. (2021).
2. Compute the poles of Norton's admittance (Equation (10)).
3. Compute the capacitances and inductances (Hollkamp's shunt: Equations (14)-(16); CF shunt: Equations (19)-(20)).
4. Compute the elastance and inductance matrices (Hollkamp's shunt: Equations (24)-(26); CF shunt: Equations (35)-(37)) and the electrical mode shapes (Equation (28)).
5. Compute the resistances (Equation (32)).

Series-parallel impedance and second Foster form tuning

The SPIS shunt proposed by Fleming et al. (2003) is shown in Figure 3b. Figure 3a features a shunt which is to the SPIS what Hollkamp's circuit is to the CF circuit. This circuit is based on the second Foster canonical form (SFCF) and can be seen as the dual of Hollkamp's circuit. The lossless circuits ($R_i = \infty$) connected in series to a capacitor are shown in Figure 4 and are used to build Thévenin's equivalent impedance Z_T. It can be recognized that the resulting circuits are equivalent to Foster's second canonical form (Chen 2018).

Tuning either type of circuit requires to compute the ZPK representation of Z_T. From Equation (4),

$$Z_T(s) = \frac{1}{sC_p^\varepsilon}\left(r_0 + \sum_{i=1}^{N_s} \frac{r_i}{\frac{s^2}{z_i^2}+1}\right)^{-1} = \frac{K}{s}\frac{\prod_{i=1}^{N_s}\left(\frac{s^2}{z_i^2}+1\right)}{\prod_{i=1}^{N_s}\left(\frac{s^2}{p_i^2}+1\right)}. \tag{38}$$

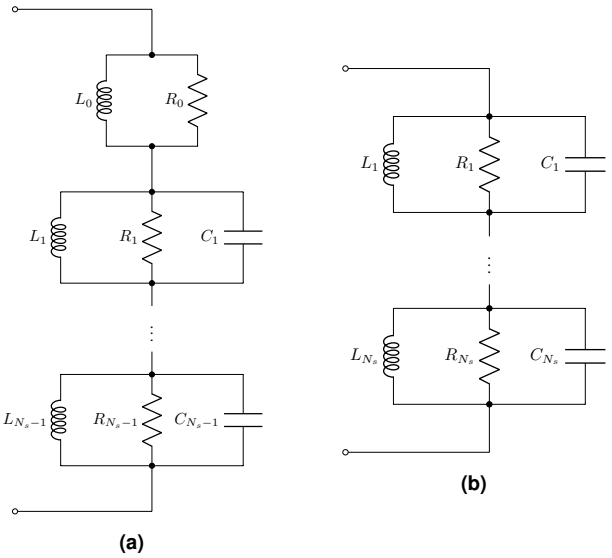

Figure 3. Shunt circuit based on the second Foster canonical form (a) and a series-parallel impedance structure (b).

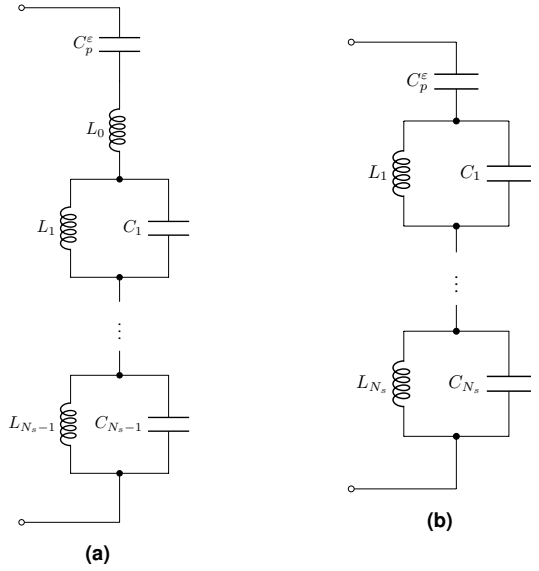

Figure 4. Thévenin's impedance model of a piezoelectric transducer connected to a lossless shunt based on the second Foster canonical form (a) and a lossless series-parallel impedance structure (b).

The poles of Thévenin's equivalent impedance can be found as the solution of the polynomial equation

$$r_0 \prod_{i=1}^{N_s}\left(\frac{s^2}{z_i^2}+1\right) + \sum_{i=1}^{N_s} r_i \prod_{k=1,k\neq i}^{N_s}\left(\frac{s^2}{z_k^2}+1\right) = 0, \tag{39}$$

which can be solved with a computer. We note that when $r_0 \neq 0$, there are N_s pairs of complex conjugate poles, whereas when $r_0 = 0$ there are $N_s - 1$. The gain K can be determined later.

Second Foster canonical form

The impedance of the undamped SFCF circuit is computed as the series connection of a capacitor, an inductor and $N_s - 1$

branches of parallel LC circuits as

$$Z_T(s) = sL_0 + \frac{1}{sC_p^\varepsilon} + \sum_{n=1}^{N_s-1} \frac{L_n s}{L_n C_n s^2 + 1} = \frac{K}{s} \frac{\prod_{i=1}^{N_s} \left(\frac{s^2}{z_i^2} + 1 \right)}{\prod_{i=1}^{N_s-1} \left(\frac{s^2}{p_i^2} + 1 \right)} \quad (40)$$

Since there are $N_s - 1$ pairs of complex conjugate poles, this circuit requires $r_0 = 0$. Evaluating the residue associated with the simple pole at $s = 0$, K is found as

$$K = \frac{1}{C_p^\varepsilon}, \quad (41)$$

and the limit for $s \to \infty$ then gives

$$L_0 = \frac{1}{C_p^\varepsilon} \frac{\prod_{i=1}^{N_s-1} p_i^2}{\prod_{i=1}^{N_s} z_i^2}. \quad (42)$$

The cover-up method enables the identification of the inductances of the LC circuits as

$$L_k = -\frac{1}{C_p^\varepsilon p_k^2} \frac{\prod_{i=1}^{N_s} \left(1 - \frac{p_k^2}{z_i^2} \right)}{\prod_{i=1, i\neq k}^{N_s-1} \left(1 - \frac{p_k^2}{p_i^2} \right)} \quad (43)$$

while the capacitances are found from the poles of the impedance as

$$C_k = \frac{1}{L_k p_k^2}. \quad (44)$$

Series-parallel impedance structure

The undamped impedance of the SPIS reads

$$Z_T(s) = \frac{1}{sC_p^\varepsilon} + \sum_{n=1}^{N_s} \frac{L_n s}{L_n C_n s^2 + 1} = \frac{K}{s} \frac{\prod_{i=1}^{N_s} \left(\frac{s^2}{z_i^2} + 1 \right)}{\prod_{i=1}^{N_s} \left(\frac{s^2}{p_i^2} + 1 \right)}, \quad (45)$$

where, using the same techniques as previously,

$$K = \frac{1}{C_p^\varepsilon}, \quad (46)$$

$$L_k = -\frac{1}{C_p^\varepsilon p_k^2} \frac{\prod_{i=1}^{N_s} \left(1 - \frac{p_k^2}{z_i^2} \right)}{\prod_{i=1, i\neq k}^{N_s} \left(1 - \frac{p_k^2}{p_i^2} \right)}, \quad (47)$$

and

$$C_k = \frac{1}{L_k p_k^2}. \quad (48)$$

It can be noted that when $r_0 \to 0$, one of the double roots of Equation (39), say, p_{N_s}, tends to infinity. Hence, Equation (48) shows that $C_{N_s} \to 0$, i.e., the capacitance tends to an open-circuit, which in Figure 3b would correspond to a topology similar to that of the SFCF shunt. Thus, as r_0 tends to zero, the SPIS shunt tends to the SFCF shunt.

Resistances tuning

A procedure completely analogous that exposed for Hollkamp's and CF shunts can be followed. In this case, the parallel RL baseline case should be chosen, because the resistors are in parallel with the inductors in the SFCF and SPIS shunts (and when $N_s = 1$, the SFCF circuit reduces to a parallel RL shunt).

Using Equation (1), the inverse of Norton's admittance is given by

$$\frac{1}{Y_{N,d}(s)} = \frac{1}{sC_p^\varepsilon + \frac{1}{Z_s(s)}} = Z_s(s) - sC_p^\varepsilon \frac{Z_s^2(s)}{1 + sC_p^\varepsilon Z_s(s)}, \quad (49)$$

where the dissipative impedance of the SFCF circuit is given by

$$Z_s(s) = \frac{1}{\frac{1}{sL_0} + \frac{1}{R_0}} + \sum_{n=1}^{N_s-1} \frac{s}{C_n s^2 + \frac{1}{R_n} s + \frac{1}{L_n}}, \quad (50)$$

or equivalently by

$$Z_s(s) = s\mathbf{1}_{1\times N_s} \left(\mathbf{B}_{SFCF} + s\mathbf{G}_{SFCF} + s^2 \mathbf{C}_{SFCF} \right)^{-1} \mathbf{1}_{N_s\times 1}, \quad (51)$$

where

$$\mathbf{C}_{SFCF} = \mathbf{diag} \begin{bmatrix} 0 & C_1 & \cdots & C_{N_s-1} \end{bmatrix}, \quad (52)$$

$$\mathbf{G}_{SFCF} = \mathbf{diag} \begin{bmatrix} R_0^{-1} & R_1^{-1} & \cdots & R_{N_s-1}^{-1} \end{bmatrix} \quad (53)$$

and

$$\mathbf{B}_{SPIS} = \mathbf{diag} \begin{bmatrix} L_0^{-1} & L_1^{-1} & \cdots & L_{N_s-1}^{-1} \end{bmatrix} \quad (54)$$

are capacitance, conductance and reluctance matrices, respectively. Once again, by comparison of Equation (49) to the Sherman-Morrison formula (Equation (95)), the inverse of Norton's admittance can be obtained after a rank-one update of the inverted matrix

$$\frac{1}{Y_{N,d}(s)} = s\mathbf{1}_{1\times N_s} \left(\mathbf{B}_{SFCF} + s\mathbf{G}_{SFCF} + s^2 \mathbf{C}_{SFCF} + s^2 \mathbf{1}_{N_s\times 1} \mathbf{1}_{1\times N_s} C_p^\varepsilon \right)^{-1} \mathbf{1}_{N_s\times 1}. \quad (55)$$

In the lossless case, the zeros of Norton's admittance are the generalized eigenvalues of the generalized eigenvalue problem

$$\mathbf{B}_{SFCF} \mathbf{\Phi}_e = \left(\mathbf{C}_{SFCF} + \mathbf{1}_{N_s\times 1} \mathbf{1}_{1\times N_s} C_p^\varepsilon \right) \mathbf{\Phi}_e \mathbf{\Omega}_e^2. \quad (56)$$

By enforcing the diagonal of the transformed matrix containing the resistances (regardless of its off-diagonal elements), the following set of resistances can be obtained:

$$\begin{bmatrix} \frac{1}{R_0} \\ \vdots \\ \frac{1}{R_{N_s-1}} \end{bmatrix} = \begin{bmatrix} \phi_{e,0,1}^2 & \cdots & \phi_{e,(N_s-1),1}^2 \\ \vdots & \ddots & \vdots \\ \phi_{e,0,N_s}^2 & \cdots & \phi_{e,(N_s-1),N_s}^2 \end{bmatrix}^{-1} \begin{bmatrix} 2\zeta_1 z_1 \\ \vdots \\ 2\zeta_{N_s} z_{N_s} \end{bmatrix}. \quad (57)$$

A similar procedure can be followed for the SPIS circuit, because its dissipative impedance

$$Z_s(s) = \sum_{n=1}^{N_s} \frac{s}{C_n s^2 + \frac{1}{R_n} s + \frac{1}{L_n}}, \tag{58}$$

is equivalently given by

$$Z_s(s) = s\mathbf{1}_{1\times N_s} \Big(\mathbf{B}_{SPIS} + s\mathbf{G}_{SPIS} + s^2 \mathbf{C}_{SPIS} \Big)^{-1} \mathbf{1}_{N_s\times 1}, \tag{59}$$

in which

$$\mathbf{C}_{SPIS} = \mathbf{diag}\begin{bmatrix} C_1 & \cdots & C_{N_s} \end{bmatrix}, \tag{60}$$

$$\mathbf{G}_{SPIS} = \mathbf{diag}\begin{bmatrix} R_1^{-1} & \cdots & R_{N_s}^{-1} \end{bmatrix} \tag{61}$$

and

$$\mathbf{B}_{SPIS} = \mathbf{diag}\begin{bmatrix} L_1^{-1} & \cdots & L_{N_s}^{-1} \end{bmatrix}. \tag{62}$$

Summary

The proposed tuning procedure for the SFCF and SPIS shunts goes as follows. Starting from a set of targeted modes and associated residues r_i,

1. Compute each frequency z_i and damping ratio ζ_i with the parallel RL baseline from the approach proposed by Raze et al. (2021).
2. Compute the poles of Thévenin's impedance (Equation (39)).
3. Compute the capacitances and inductances (SFCF shunt: Equations (42)-(44); SPIS shunt: Equations (47)-(48)).
4. Compute the capacitance and reluctance matrices (SFCF shunt: Equations (52)-(54); SPIS shunt: Equations (60)-(62)) and the electrical mode shapes (Equation (56)).
5. Compute the resistances (Equation (57)).

Current blocking shunt circuit tuning

The CB shunt was originally proposed by Wu (1998), and later simplified by Agneni et al. (2006). A different tuning methodology was proposed by Raze et al. (2020), and will be compared to that proposed herein in the numerical examples. Once again, the dynamics of the lossless circuit are first analyzed to assess the electromechanical coupling, and the tuning of dissipative circuits is considered afterwards.

Lossless circuit tuning

Figure 6 features Norton's admittance model using a lossless CB shunt, which is identical for CB circuits with series and parallel shunts. The resulting circuit is composed of a parallel capacitor, followed by a repetition of $N_s - 1$ stages with identical topology (a shunt with an inductor and a branch with a parallel LC circuit) and finally terminated by an inductor. The parallel LC circuits are so-called current-blocking filters, because they act as band-stop filters. Indeed, their impedance is given by

$$\tilde{Z}_i = \frac{1}{\frac{1}{\tilde{L}_i s} + s\tilde{C}_i} \tag{63}$$

and becomes infinite at $s = j\sqrt{1/(\tilde{L}_i\tilde{C}_i)}$. Hence, by properly setting the blocking frequency of these filters, it is possible to decouple some parts of the circuits at specific frequencies.

The tuning approach traditionally chosen for the CB shunt thus consists in considering sequentially each stage in ascending order (Wu 1998; Agneni et al. 2006; Raze et al. 2020). By tuning the filter of the considered stage to the frequency of the targeted resonance, the influence of the following stages of unknown characteristics can be neglected close to that frequency, and the shunt can be tuned taking into account the rest of the circuit (the piezoelectric capacitance and previous stages of known characteristics). The procedure can be repeated until all stages have been tuned.

Figure 7 shows a representation of the tuning considerations for stage k. The shunt impedances and current blocking filters are represented up to stage k, whereas the remainder of the CB circuit is represented altogether with the impedance Z_{k+1}. The voltage across the shunt inductance k is noted V_k and the current entering stage k is noted I_k.

The relations between V_p, I_p, V_k and I_k can be obtained using the two-port network theory (Alexander and Sadiku 2000). These relations are expressed with a transfer matrix $\mathbf{H}_{CB}^{(k)}$ by

$$\begin{bmatrix} V_p \\ I_p \end{bmatrix} = \mathbf{H}_{CB}^{(k)}(s) \begin{bmatrix} V_k \\ I_k \end{bmatrix} = \begin{bmatrix} h_{11}^{(k)}(s) & h_{12}^{(k)}(s) \\ h_{21}^{(k)}(s) & h_{22}^{(k)}(s) \end{bmatrix} \begin{bmatrix} V_k \\ I_k \end{bmatrix}. \tag{64}$$

The expression of the transfer matrix results from the cascade connection of the parallel capacitor, and stages 1 to $k-1$ and is given by (Raze et al. 2020)*

$$\mathbf{H}_{CB}^{(k)}(s) = \begin{bmatrix} 1 & 0 \\ sC_p^{\varepsilon} & 1 \end{bmatrix} \prod_{i=1}^{k-1} \begin{bmatrix} 1 & \frac{\frac{1}{\tilde{C}_i}s}{s^2 + \frac{1}{\tilde{L}_i\tilde{C}_i}} \\ \frac{1}{L_i s} & 1 + \frac{\frac{1}{\tilde{C}_i}s}{s^2 + \frac{1}{\tilde{L}_i\tilde{C}_i}} \frac{1}{L_i s} \end{bmatrix}. \tag{65}$$

The relation between I_k and V_k can be deduced from Figure 7 as

$$\frac{I_k}{V_k} = Y_k(s) = \frac{1}{L_k s} + \frac{1}{\frac{\frac{1}{\tilde{C}_k}s}{s^2 + \frac{1}{\tilde{L}_k\tilde{C}_k}} + Z_{k+1}(s)}. \tag{66}$$

*What is termed transfer matrix in this article is the inverse of what is termed transfer matrix in Raze et al. (2020).

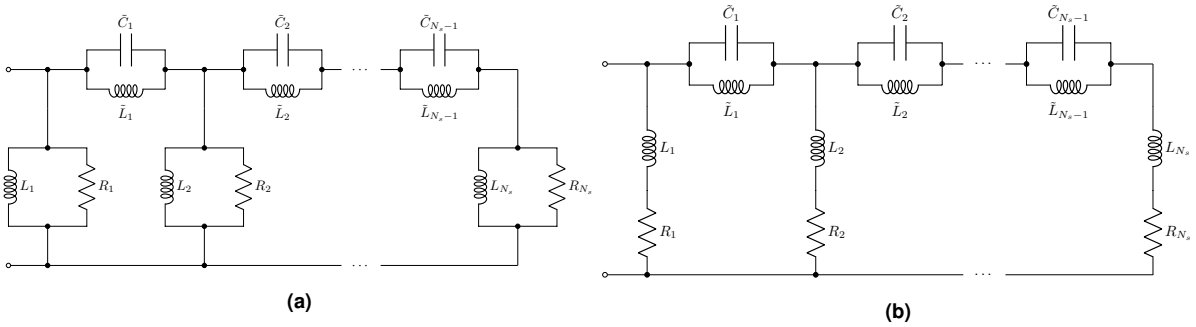

Figure 5. Simplified current blocking shunt with parallel RL shunts (a) and series RL shunts (b).

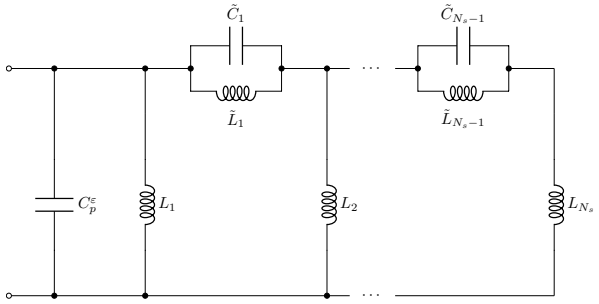

Figure 6. Norton's admittance model of a piezoelectric transducer connected to a lossless current blocking shunt.

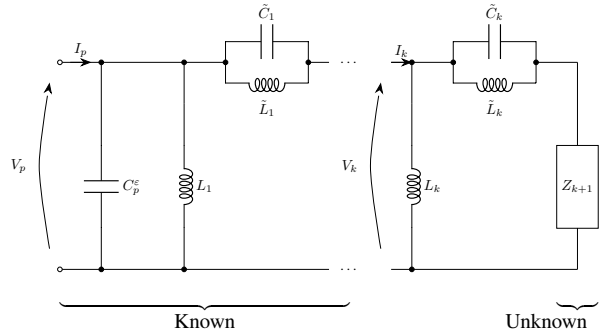

Figure 7. Norton's admittance model of a piezoelectric transducer connected to a lossless current blocking shunt: tuning considerations at stage k.

The relation between I_p and V_p, i.e. Norton's equivalent admittance, is then deduced from Equations (64) and (66) as

$$Y_N(s) = \frac{I_p}{V_p} = \frac{h_{22}^{(k)}(s)Y_k(s) + h_{21}^{(k)}(s)}{h_{12}^{(k)}(s)Y_k(s) + h_{11}^{(k)}(s)}. \tag{67}$$

A zero of Norton's admittance occurs if

$$Y_N(jz_k) = 0. \tag{68}$$

The problem can be made independent of Z_{k+1} if the current blocking filter has an infinite impedance at z_k. This is the case if

$$\tilde{L}_k = \frac{1}{z_k^2 \tilde{C}_k}. \tag{69}$$

Equation (66) then becomes at $s = jz_k$

$$Y_k(jz_k) = \frac{1}{jz_k L_k}. \tag{70}$$

Solving Equation (68) with Equations (67) and (70) yields

$$L_k = -\frac{1}{jz_k}\frac{h_{22}^{(k)}(jz_k)}{h_{21}^{(k)}(jz_k)}. \tag{71}$$

This tuning approach guarantees that Norton's admittance will have a zero at the desired frequency regardless of Z_{k+1}. We note that L_k is solely determined by z_k, and the piezoelectric capacitance as well as the characteristics from the previous stages condensed in the transfer matrix. A free parameter yet remains for the lossless case, as the two parameters of the current blocking filter are only constrained by one relation given in Equation (69). It shall be shown next that the filter capacitance is actually set by the value of the residue r_k.

Coupling assessment

Norton's equivalent admittance is such that

$$\frac{s}{Y_N(s)} = \frac{1}{C_p^\varepsilon}\sum_{i=1}^{N_s}\frac{s^2 r_i}{s^2 + z_i^2}. \tag{72}$$

Thus, the residue r_k may be evaluated with Equations (66) and (67) thanks to the cover-up method as

$$\begin{aligned} r_k &= \lim_{s\to jz_k} C_p^\varepsilon (s^2 + z_k^2)\frac{1}{sY_N(s)} \\ &= \lim_{s\to jz_k} C_p^\varepsilon (s^2 + z_k^2)\frac{h_{12}^{(k)}(s)Y_k(s) + h_{11}^{(k)}(s)}{sh_{22}^{(k)}(s)Y_k(s) + sh_{21}^{(k)}(s)} \\ &= \lim_{s\to jz_k} C_p^\varepsilon \frac{\dfrac{h_{12}^{(k)}(s)}{L_k s} + h_{11}^{(k)}(s)}{\dfrac{\dfrac{h_{22}^{(k)}(s)}{L_k} + sh_{21}^{(k)}(s)}{s^2 + z_k^2} + h_{22}^{(k)}(s)\tilde{C}_k}. \end{aligned} \tag{73}$$

Hence, the impedance of the next stages $Z_{k+1}(s)$ has no influence on the residue (provided that Equation (69) holds). This is a more formal justification of the equivalent physically-motivated assumption made in Raze et al. (2020). However, the residue remains rather uneasy to compute in that way, because no further simplification can be made in general when considering the full CB circuit.

Equation (73) shows that the residue computed considering the whole CB circuit would be identical to that computed when considering $Z_{k+1} = 0$, i.e., by replacing the next stages by a short circuit, as pictured in Figure 8. The fact

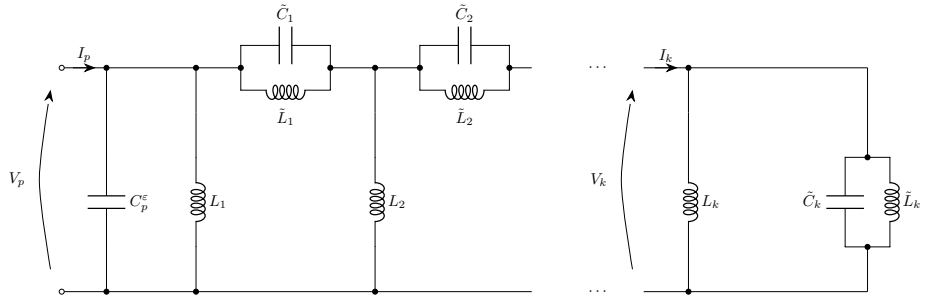

Figure 8. Norton's admittance model of a piezoelectric transducer connected to a lossless current blocking shunt: simplified tuning considerations at stage k.

that $Z_{k+1}(s)$ can be considered as a short circuit and that Norton's equivalent admittance has as zeros $z_1, \cdots, z_k$ leads to the following expression (Equation (67))

$$\frac{1}{C_p^\varepsilon}\sum_{i=1}^{k}\frac{r_i s^2}{s^2+z_i^2} = s\frac{h_{12}^{(k)}(s)\left(\frac{1}{L_k s}+\tilde{C}_k\frac{s^2+z_k^2}{s}\right)+h_{11}^{(k)}(s)}{h_{22}^{(k)}(s)\left(\frac{1}{L_k s}+\tilde{C}_k\frac{s^2+z_k^2}{s}\right)+h_{21}^{(k)}(s)}. \quad (74)$$

Taking the limit as $s\to\infty$, the sum of residues can be evaluated

$$\sum_{i=1}^{k} r_i = \lim_{s\to\infty} sC_p^\varepsilon \frac{h_{12}^{(k)}(s)\left(\frac{1}{L_k s}+\tilde{C}_k\frac{s^2+z_k^2}{s}\right)+h_{11}^{(k)}(s)}{h_{22}^{(k)}(s)\left(\frac{1}{L_k s}+\tilde{C}_k\frac{s^2+z_k^2}{s}\right)+h_{21}^{(k)}(s)}. \quad (75)$$

To evaluate this limit, the asymptotic behavior of the two-port network must be determined. Taking the limit as $s\to\infty$, the following asymptotic behaviors can be derived from Equation (65)

$$\lim_{s\to\infty}\begin{bmatrix} h_{11}^{(k)}(s) & h_{12}^{(k)}(s) \\ h_{21}^{(k)}(s) & h_{22}^{(k)}(s)\end{bmatrix} = \lim_{s\to\infty}\begin{bmatrix} 1 & \sum_{i=1}^{k-1} 1/(s\tilde{C}_i) \\ sC_p^\varepsilon & 1+\sum_{i=1}^{k-1} C_p^\varepsilon/\tilde{C}_i\end{bmatrix}. \quad (76)$$

The network associated with such a transfer matrix is depicted in Figure 9. Intuitively, the components governing this asymptotic behavior are the capacitances, because the inductances tend to have a much higher impedance at high frequency ($s\to\infty$). In fact, Figure 9 can be obtained from Figure 8 after replacing the inductances by open circuits.

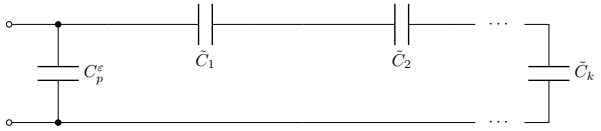

Figure 9. Asymptotic behavior of the current blocking shunt simplified at stage k for $s\to\infty$.

Inserting Equation (76) into Equation (75), the sum of residues can then be evaluated as

$$\sum_{i=1}^{k} r_i = \lim_{s\to\infty} sC_p^\varepsilon \frac{\sum_{i=1}^{k-1}\frac{1}{s\tilde{C}_i}\left(\frac{1}{L_k s}+\tilde{C}_k\frac{s^2+z_k^2}{s}\right)+1}{\left(1+\sum_{i=1}^{k-1}\frac{C_p^\varepsilon}{\tilde{C}_i}\right)\left(\frac{1}{L_k s}+\tilde{C}_k\frac{s^2+z_k^2}{s}\right)+sC_p^\varepsilon} = \frac{1+\sum_{i=1}^{k-1}\frac{\tilde{C}_k}{\tilde{C}_i}}{1+\frac{\tilde{C}_k}{C_p^\varepsilon}+\sum_{i=1}^{k-1}\frac{\tilde{C}_k}{\tilde{C}_i}} \quad (77)$$

A remarkable feature of this equation is that the residues depend only on the filter and piezoelectric capacitances. By extracting $\tilde{C}_k$, it is expressed as

$$\tilde{C}_k = \frac{1-\sum_{i=1}^{k} r_i}{\sum_{i=1}^{k} r_i\left(\frac{1}{C_p^\varepsilon}+\sum_{i=1}^{k-1}\frac{1}{\tilde{C}_i}\right)-\sum_{i=1}^{k-1}\frac{1}{\tilde{C}_i}}, \quad (78)$$

or as a sole function of the residues and the piezoelectric capacitance

$$\tilde{C}_k = \frac{C_p^\varepsilon}{\frac{\sum_{i=1}^{k} r_i}{1-\sum_{i=1}^{k} r_i}+\sum_{l=1}^{k-1}(-1)^{k-l}\frac{\sum_{i=1}^{l} r_i}{1-\sum_{i=1}^{l} r_i}}. \quad (79)$$

Dissipative circuit tuning with parallel RL shunts

The case of a dissipative CB shunt is now considered. In case parallel RL shunts are used as in Figure 5a, the parallel RL baseline should be used. The transfer matrix resulting in a cascade connection of a parallel capacitance C_p^ε and the

$k-1$ first stages of the current blocking circuit reads

$$\mathbf{H}_{CB}^{(k)} = \begin{bmatrix} 1 & 0 \\ sC_p^{\varepsilon} & 1 \end{bmatrix} \prod_{i=1}^{k-1} \begin{bmatrix} 1 & \dfrac{\frac{1}{\tilde{C}_i}s}{s^2+\frac{1}{\tilde{L}_i\tilde{C}_i}} \\ \dfrac{1}{L_is}+\dfrac{1}{R_i} & 1+\dfrac{\frac{1}{\tilde{C}_i}s}{s^2+\frac{1}{\tilde{L}_i\tilde{C}_i}}\left(\dfrac{1}{L_is}+\dfrac{1}{R_i}\right) \end{bmatrix}. \quad (80)$$

Using Equations (7) and (67), Norton's dissipative admittance can be equated to its nominal value at $s = jz_k$

$$\begin{aligned} Y_{N,d}(jz_k) &= -\sum_{i=1}^{N_s} \frac{r_i z_k^2}{z_i^2 + 2j\zeta_i z_i z_k - z_k^2} \\ &= \frac{h_{22}^{(k)}(jz_k)Y_k(jz_k) + h_{21}^{(k)}(jz_k)}{h_{12}^{(k)}(jz_k)Y_k(jz_k) + h_{11}^{(k)}(jz_k)}. \end{aligned} \quad (81)$$

Extracting $Y_k(jz_k)$ from this relation yields

$$Y_k(jz_k) = \frac{h_{11}^{(k)}(jz_k)Y_{N,d}(jz_k) - h_{21}^{(k)}(jz_k)}{h_{22}^{(k)}(jz_k) - h_{12}^{(k)}(jz_k)Y_{N,d}(jz_k)}, \quad (82)$$

which sets the ideal value of $Y_k(jz_k)$. If the filter capacitance and inductance are properly tuned (Equations (79) and (69), respectively), the admittance Y_k evaluated at the frequency z_k is then only determined by the k^{th} shunt

$$\begin{aligned} &Y_k(jz_k) \\ &= \frac{1}{jL_kz_k} + \frac{1}{R_k} + \frac{\frac{1}{\tilde{L}_k\tilde{C}_k} - z_k^2}{\frac{1}{j\tilde{C}_kz_k} + \left(\frac{1}{\tilde{L}_k\tilde{C}_k} - z_k^2\right) Z_{k+1}(jz_k)} \\ &= \frac{1}{jL_kz_k} + \frac{1}{R_k}, \end{aligned} \quad (83)$$

so that the inductance and resistance can be set as

$$L_k = -\frac{1}{z_k \Im\{Y_k(jz_k)\}} \quad (84)$$

and

$$R_k = \frac{1}{\Re\{Y_k(jz_k)\}}, \quad (85)$$

respectively.

Dissipative circuit tuning with series RL shunts

When series RL shunts are used as in Figure 5b, the series RL baseline should be used. The transfer matrix resulting in a cascade connection of a series capacitance C_p^{ε} and the $k-1$ first stages of the current blocking circuit reads

$$\mathbf{H}_{CB}^{(k)} = \begin{bmatrix} 1 & \dfrac{1}{sC_p^{\varepsilon}} \\ 0 & 1 \end{bmatrix} \prod_{i=1}^{k-1} \begin{bmatrix} 1 & \dfrac{\frac{1}{\tilde{C}_i}s}{s^2+\frac{1}{\tilde{L}_i\tilde{C}_i}} \\ \dfrac{1}{L_is+R_i} & 1+\dfrac{\frac{1}{\tilde{C}_i}s}{s^2+\frac{1}{\tilde{L}_i\tilde{C}_i}}\dfrac{1}{L_is+R_i} \end{bmatrix}. \quad (86)$$

Taking the inverse of Equation (66), Thévenin's impedance can be equated to its nominal value

$$\begin{aligned} Z_{T,d}(jz_k) &= \sum_{i=1}^{N_s} \frac{r_i}{1 + 2j\zeta_i\frac{z_k}{z_i} - \frac{z_k^2}{z_i^2}} \\ &= \frac{h_{12}^{(k)}(jz_k)Y_k(jz_k) + h_{11}^{(k)}(jz_k)}{h_{22}^{(k)}(jz_k)Y_k(jz_k) + h_{21}^{(k)}(jz_k)}, \end{aligned} \quad (87)$$

and thus, Y_k at $s = jz_k$ should be given by

$$Y_k(jz_k) = \frac{h_{11}^{(k)}(jz_k) - h_{21}^{(k)}(jz_k)Z_{T,d}(jz_k)}{h_{22}^{(k)}(jz_k)Z_{T,d}(jz_k) - h_{12}^{(k)}(jz_k)}, \quad (88)$$

which sets the ideal value of $Y_k(jz_k)$. If the filter capacitance and inductance are properly tuned (Equations (79) and (69), respectively), the admittance Y_k evaluated at the frequency z_k is once again only determined by the k^{th} shunt

$$\begin{aligned} &Y_k(jz_k) \\ &= \frac{1}{jL_kz_k + R_k} + \frac{\frac{1}{\tilde{L}_k\tilde{C}_k} - z_k^2}{\frac{1}{j\tilde{C}_kz_k} + \left(\frac{1}{\tilde{L}_k\tilde{C}_k} - z_k^2\right) Z_{k+1}(jz_k)} \\ &= \frac{1}{jL_kz_k + R_k}, \end{aligned} \quad (89)$$

so that the inductance and resistance can be set as

$$L_k = \frac{1}{z_k}\Im\left\{\frac{1}{Y_k(jz_k)}\right\} \quad (90)$$

and

$$R_k = \Re\left\{\frac{1}{Y_k(jz_k)}\right\}, \quad (91)$$

respectively.

Summary

The proposed tuning procedure for the CB shunt goes as follows. Starting from a set of targeted modes and associated residues r_i,

1. Compute each frequency z_i and damping ratio ζ_i with the series or parallel RL baseline from the approach proposed by Raze et al. (2021) for the CB shunt with series or parallel shunts, respectively.

2. Compute the filters capacitances and inductances (Equations (79) and (69)).
3. For each stage, compute sequentially the transfer matrix (series shunts: Equation (86); parallel shunts: Equation (80)), the ideal value of Y_k (series shunts: Equations (87)-(88) ; parallel shunts: Equations (81)-(82)) and the shunt resistance and inductance (series shunts: Equations (90)-(91); parallel shunts: Equations (84)-(85)).

Numerical verification of the tuning procedure

The clamped-free piezoelectric beam depicted in Figure 10 is considered as an example to illustrate the tuning procedure. The free end of the beam is attached to a thin lamina. The geometrical and material characteristics of the beam are reported in Table 1. The beam is excited transversally 20 cm away from the clamped end, and its displacement is computed at the same location. The thin lamina can be responsible for a hardening nonlinear behavior of the system (Lossouarn et al. 2018). However, the forcing levels considered in this study are low enough to make this effect negligible, and the beam is assumed to behave linearly.

The beam is covered over its whole length by ten piezoelectric cells. Each cell consists of four PSI-5A4E piezoelectric patches, placed symmetrically in stacks of two on either side of the beam. The wiring of the patches is depicted in Figure 10a, and their geometrical and material characteristics are reported in Table 2.

The finite element method proposed by Thomas et al. (2009) was used with Euler-Bernoulli beam elements to obtain a numerical model of the beam. The beam and lamina were discretized with one element per millimeter. Accounting for the clamped boundary conditions and the attachment between the beam and lamina, this resulted in a model with 4437 degrees of freedom. To keep the analysis tractable, a Craig-Bampton-based model order reduction technique proposed by Raze (2021) was used, retaining one interface mechanical degree of freedom and twenty component normal modes, as well as the electrical degrees of freedom of all patches. Modal damping of 0.2% was added to the model to replicate the experimental results.

The first two modes are targeted in this section to simply illustrate the trade-offs involved by the choice of the residues, and their impact on performance. To obtain maximal yet balanced coupling on these modes, the first two piezoelectric cells are connected in parallel, and the other cells are left in open circuit. To give an idea of the orders of magnitude, Table 3 lists the resistances and inductances of series and parallel RL shunts targeting mode one or two.

Hollkamp's shunt circuit

To check the tuning approach for Hollkamp's shunt, various values for the residues were considered for r_1 and $r_2 = 1 - r_1$ (Equation (6)). Figure 11 features the resulting frequency response functions (FRFs) and Table 4 gathers the associated electrical parameters. A large value for r_1 (r_2) leads to a better reduction of mode one (two). A problematic case is nonetheless observed for $r_1 = 0.1$; it can also be observed in Table 4 that R_0 is negative for this case.

The apparent issue with $r_1 = 0.1$ and $r_2 = 0.9$ is due to the physical behavior of the circuit in this configuration. This behavior is illustrated in Figure 12, where the resistance in either branch is varied while the other one is maintained at zero. On the one hand, from Figure 12a, it can be seen that R_0 has a moderate effect on mode 2, but can be tuned to optimally damp mode one. On the other hand Figure 12b indicates that R_1 has a significant effect on mode 2. However, its effect is even more pronounced on mode 1, and when mode 2 is optimally damped mode 1 is overdamped. This stems from the ability of series RL shunts to damp lower-frequency modes (Berardengo et al. 2021). From this setting, the tuning method seeks to retrieve a correct damping on mode 1 (and barely affect that on mode 2) by setting R_0 to a negative value. Hence, there does not seem to exist a set of positive resistances that optimally damp modes 1 and 2 simultaneously in this configuration. This rules out this circuit for practical implementation in this case. Indeed, a passive resistor with negative resistance does not exist. Even when using analog or digital circuits to emulate the shunt, the implementation is strongly inadvisable, as the equivalent controller would be unstable. In general, it was observed by the authors that Hollkamp's shunt is suited for emphasis on lower-frequency modes, but may perform poorly if emphasis is put on higher-frequency modes, and a rule of thumb should be to use this circuit with residues satisfying $r_{k+1} \leq r_k$ ($k = 1, \cdots, N_s - 1$), but the problem also depends on the coupling with each mode. In any case, a verification of the electrical parameters is advisable.

Second Foster form

Figure 13 depicts the FRFs of the beam controlled with an SFCF shunt, and Table 5 gathers the associated electrical parameters. Besides problematic cases, the performance in terms of vibration reduction is similar to that of Hollkamp's shunt if the same set of residues is considered.

An issue with $r_1 = 0.9$ is observable in Figure 13. As can be seen in Table 5, this is due to a negative resistance. This issue is similar to the one occurring with Hollkamp's shunt, and it can be shown that it comes from the physical behavior of the circuit in this configuration as well. The difference of this case with Hollkamp's shunt is that is appears when emphasis is put on the lower-frequency mode, which stems from the ability of parallel RL shunts to damp higher-frequency modes (Berardengo et al. 2021). It was observed by the authors that, conversely to Hollkamp's shunt, the SFCF circuit is suited for emphasis on higher-frequency modes, but may perform poorly if emphasis is put on lower-frequency modes, and a rule of thumb should be to use this circuit with residues satisfying $r_{k+1} \geq r_k$ ($k = 1, \cdots, N_s - 1$), but a verification of the electrical parameters is also advisable.

Current flowing and series-parallel impedance structure

The performance of the CF and SPIS shunts is investigated in Figure 14 for various values of r_0 and by setting $r_1 = r_2 = (1 - r_0)/2$ (Equation (6)). For reference, Hollkamp's and an SFCF shunts are also used with $r_1 = r_2 = 0.5$. As expected from the theoretical analysis, the CF and SPIS

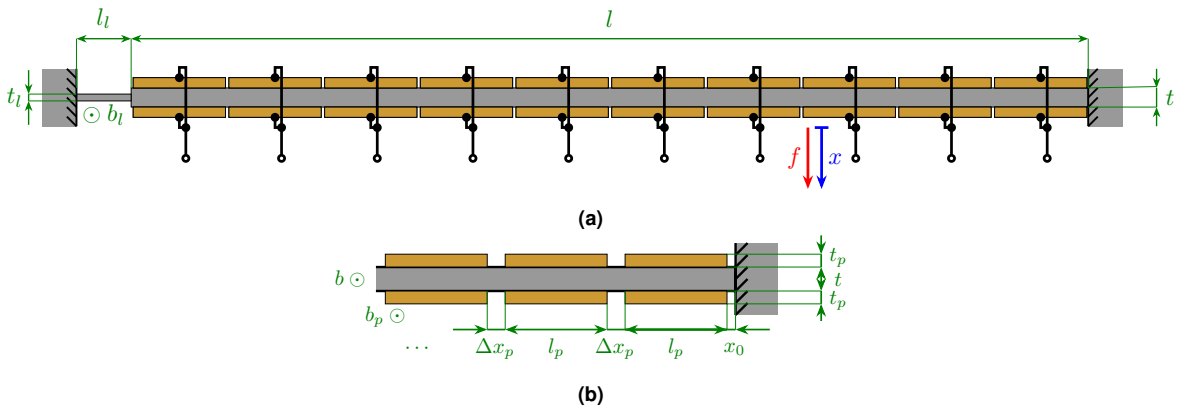

Figure 10. Schematic representation of the clamped-free piezoelectric beam with a thin lamina: overall view (a) and close-up on the patches close to the clamped end (b).

Table 1. Parameters of the clamped-free piezoelectric beam with a thin lamina.

l	b	t	l_l	b_l	t_l	ρ	E
700 mm	14 mm	14 mm	40 mm	14 mm	0.5 mm	7850 kg/m^3	210 GPa

Table 2. Parameters of the piezoelectric patches of the clamped-free piezoelectric beam with a thin lamina (ϵ_0=8.854 pF/m).

l_p	b_p	t_p	x_0	Δx_p	ρ_p	E_p	d_{31}	$\epsilon^{\varepsilon}_{33}$
67 mm	14 mm	2 mm	1 mm	3 mm	7800 kg/m^3	66 GPa	-190$\times$10^{-12}m/V	1531ϵ_0

Table 3. Parameters of series (a) and parallel (b) single-mode RL shunts.

Mode	R	L
1	7.51 kΩ	229.08 H
2	1.15 kΩ	9.92 H

(a)

Mode	R	L
1	301.03 kΩ	234.91 H
2	85.14 kΩ	10.06 H

(b)

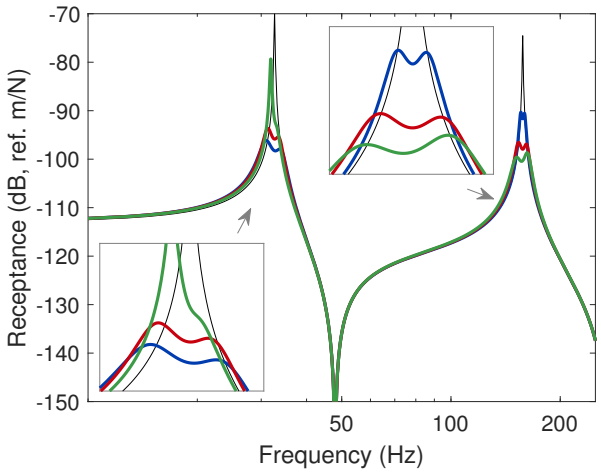

Figure 11. FRF of the beam with open-circuited patches (—) and controlled with Hollkamp's shunt: $r_1 = 0.9$, $r_2 = 0.1$ (—), $r_1 = 0.5$, $r_2 = 0.5$ (—) and $r_1 = 0.1$, $r_2 = 0.9$ (—).

circuits performance tends to approach that of Hollkamp's and the SFCF shunts, respectively, when $r_0 \to 0$. When $r_0 \to 1$, the passivity constraint imposes that $r_1 \to 0$ and $r_2 \to 0$, i.e., the control authority over the first and second modes gradually vanishes.

The electrical parameters as functions of r_0 (keeping $r_1 = r_2 = (1 - r_0)/2$) are plotted in Figure 15. Two asymptotic states for the CF can be identified. As $r_0 \to 0$, the capacitance in the first branch tends to infinity, i.e., to a short-circuit, and the CF circuit becomes equivalent to Hollkamp's circuit. When $r_0 \to 1$, the capacitances tend to zero while the resistances and inductances tend to infinity, i.e., the CF globally tends to an open-circuit. Similarly, two asymptotic states for the SPIS can be identified: the SFCF circuit when $r_0 \to 0$, and a short-circuit when $r_0 \to 1$. This latter state has the practical advantage that the inductances are quite small when $r_0 \lesssim 1$, and it was what motivated its introduction in Fleming et al. (2003). However, this comes at the expense of higher capacitances and reduced performance on the controlled modes.

Figure 15d also features the resonance frequencies of the branches of the lossless circuits, i.e., $\sqrt{1/(C_n L_n)}$. These resonance frequencies are compared to the tuning rules proposed in the works first proposing the CF (Behrens et al. 2003) and SPIS (Fleming et al. 2003) shunts, considering that the capacitances are equal to those given by the proposed tuning approach, and that the inductances are computed with the methods therein. For the CF circuit, the tuning rules agree well for large r_0, but a substantial error is made using the rules in Behrens et al. (2003) for small r_0. According to Figure 15a, small r_0 correspond to high capacitances, which is desirable from a vibration reduction point of view in this case, as discussed in Cigada et al. (2012). It was also identified therein that the issue comes from a strong interaction between the branches, whereas in Behrens et al. (2003) they are tuned independently. A similar observation can be made for the SPIS circuit, but the discrepancy is larger for large r_0 in this case. This is simply due to the fact that the circuit is tuned to the open-circuit resonance frequencies in Fleming et al. (2003), whereas it is tuned to the short-circuit ones herein. To

Table 4. Parameters of Hollkamp's shunt.

	R_0	L_0	C_1	R_1	L_1
$r_1 = 0.9$, $r_2 = 0.1$	6.45 kΩ	207.82 H	10.28 nF	3.96 kΩ	109.51 H
$r_1 = 0.5$, $r_2 = 0.5$	2.49 kΩ	121.34 H	86.06 nF	1.90 kΩ	22.65 H
$r_1 = 0.1$, $r_2 = 0.9$	-1.63 kΩ	32.51 H	443.48 nF	2.82 kΩ	16.58 H

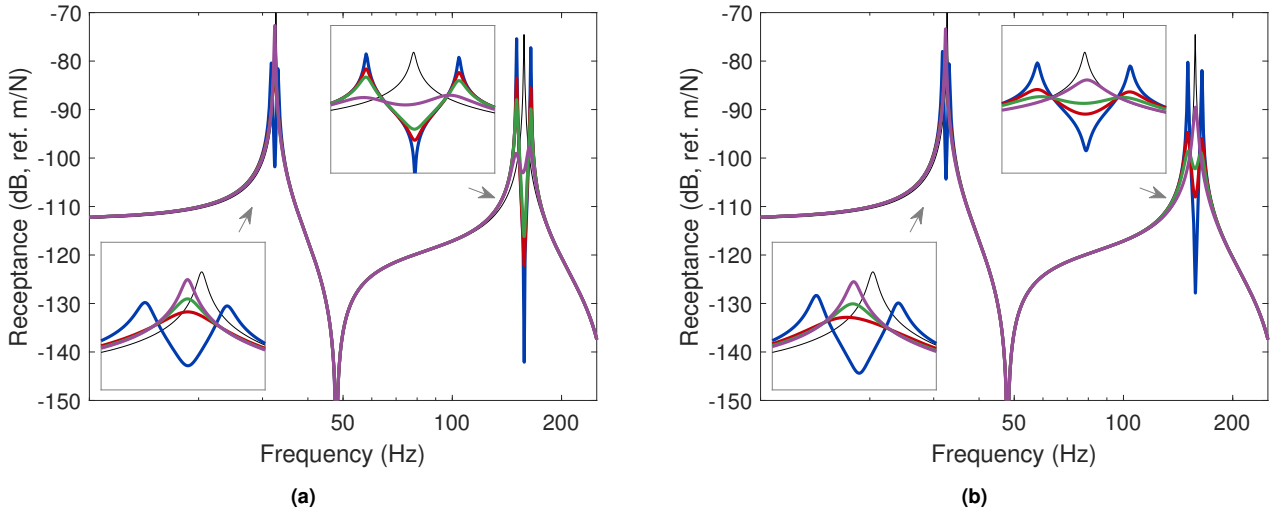

Figure 12. FRF of the beam with open-circuited patches (—) and controlled with Hollkamp's shunt ($r_1 = 0.1$, $r_2 = 0.9$): $R_1 = 0$ and $R_0 = 100\ \Omega$ (—), $R_0 = 1$ kΩ (—), $R_0 = 2$ kΩ (—) and $R_0 = 10$ kΩ (—) (a); $R_0 = 0$ and $R_1 = 100\ \Omega$ (—), $R_1 = 1$ kΩ (—), $R_1 = 2$ kΩ (—) and $R_1 = 10$ kΩ (—) (b).

Table 5. Parameters of the SFCF shunt.

	R_0	L_0	C_1	R_1	L_1
$r_1 = 0.9$, $r_2 = 0.1$	-181.10 kΩ	72.24 H	23.65 nF	119.25 kΩ	140.32 H
$r_1 = 0.5$, $r_2 = 0.5$	309.82 kΩ	19.22 H	121.06 nF	180.33 kΩ	103.64 H
$r_1 = 0.1$, $r_2 = 0.9$	99.89 kΩ	11.11 H	1.01 μF	86.59 kΩ	21.57 H

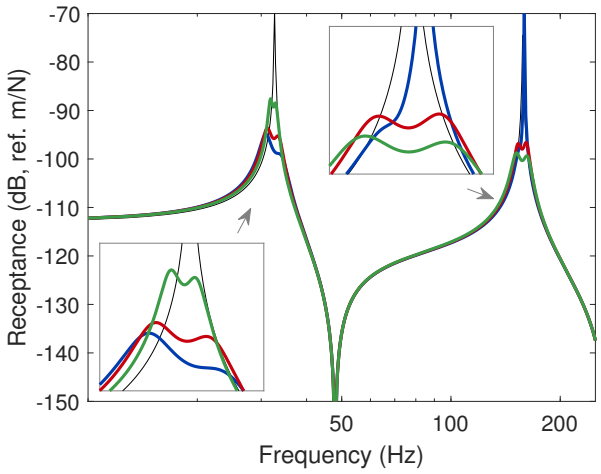

Figure 13. FRF of the beam with open-circuited patches (—) and controlled with an SFCF shunt: $r_1 = 0.9$, $r_2 = 0.1$ (—), $r_1 = 0.5$, $r_2 = 0.5$ (—) and $r_1 = 0.1$, $r_2 = 0.9$ (—).

conclude the comparison, it should also be pointed out that no quantitative selection method for the capacitances in the circuit was proposed in Behrens et al. (2003); Fleming et al. (2003), while in this paper they are deduced from the residues. Furthermore, the resistances tuning was carried out using numerical optimization therein (Fleming et al. 2002), whereas the proposed approach uses directly formulas from the single-mode case (Raze et al. 2021).

Current blocking shunt circuit

The last cases are the CB circuits with series and parallel RL shunts. For these circuits, a comparison with the tuning approach proposed in Raze et al. (2020) is performed.

Figure 16 shows the FRFs of the beam controlled with CB shunts of both types (with series and parallel RL shunts) tuned with either approach. The parameters of the CB shunts with series and parallel RL shunts obtained with the proposed approach are given in Tables 6 and 7, respectively. The filter capacitances were determined with the approach in this article, and were used as an input for the method in Raze et al. (2020). There exist slight differences (which are larger for parallel RL shunts on the second mode), but the performance and trends in terms of vibration mitigation are essentially the same. Furthermore, by comparing Figures 11, 13 and 16, it can be observed that (besides problematic cases) vibration reduction is nearly identical for all circuits and is determined solely by the residues.

The approach proposed in this work has several advantages over the one proposed in Raze et al. (2020). It is more generic, as it can be extended to other shunts. It is easier to implement and provides more insight, namely it requires as input the residues whose connection with the MEMCF has been established, whereas the approach in Raze et al. (2020) requires the filter capacitance values, whose impact on coupling is less straightforward to assess (Equation (79)). Finally, it decouples the identification procedure from the tuning procedure, which permits to use

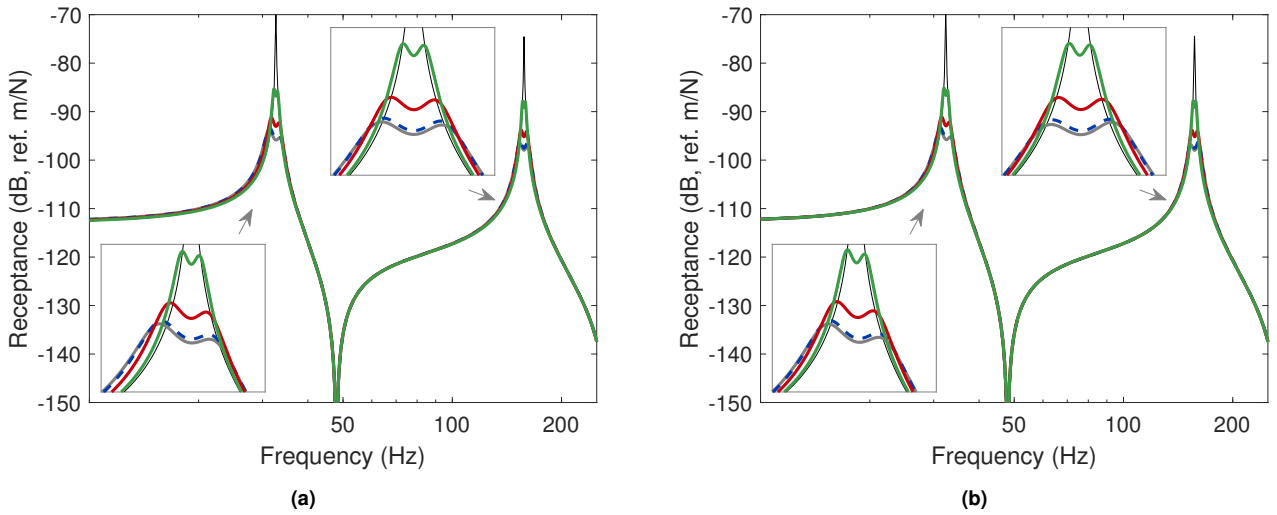

Figure 14. (a): FRF of the beam with open-circuited patches (—) and controlled with Hollkamp's shunt (—) and a CF shunt with $r_0 = 0.1$ (- - -), $r_0 = 0.5$ (—) and $r_0 = 0.9$ (—). (b): FRF of the beam with short-circuited patches (—) and controlled with an SFCF shunt (—) and an SPIS shunt with $r_0 = 0.1$ (- - -), $r_0 = 0.5$ (—) and $r_0 = 0.9$ (—).

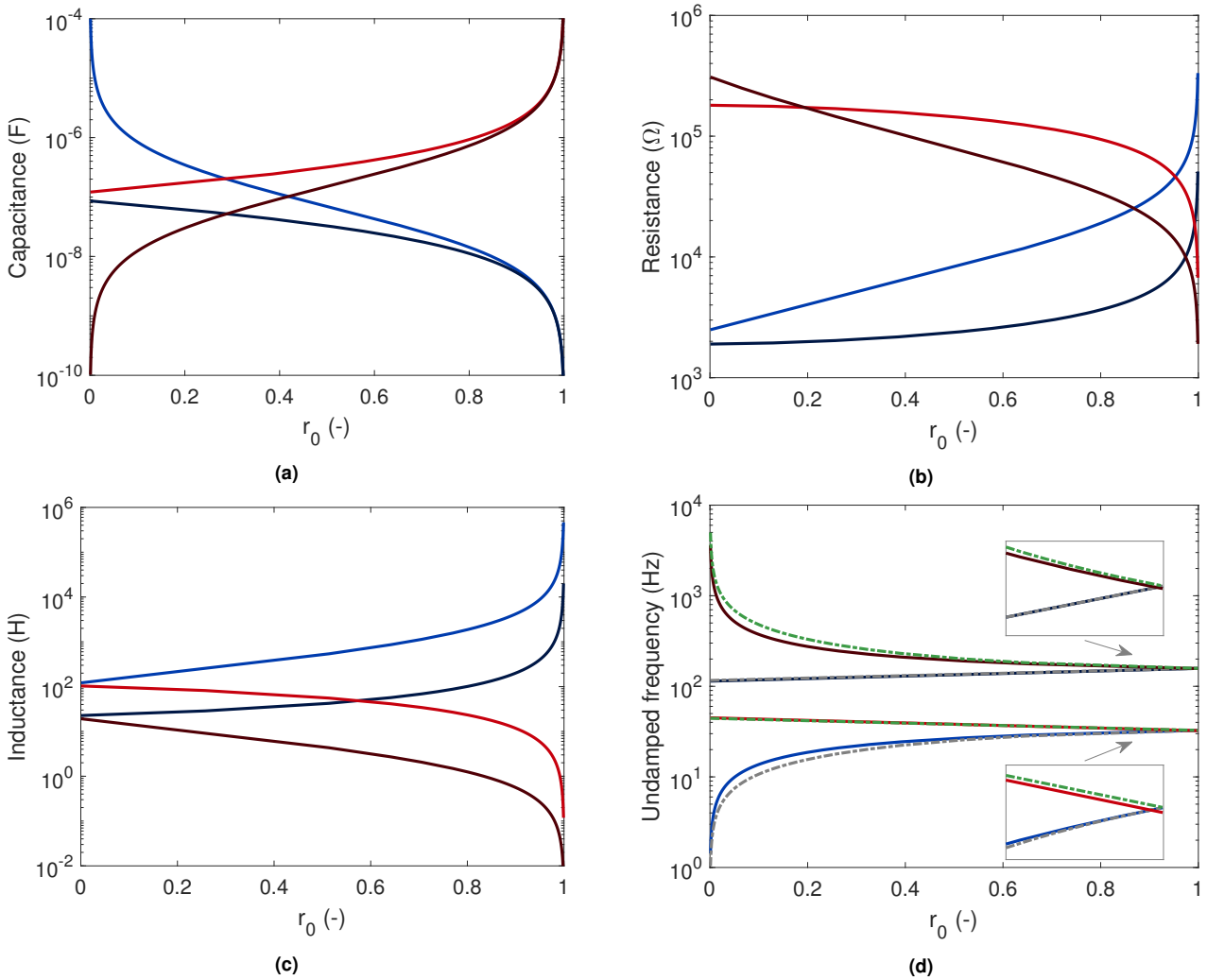

Figure 15. Capacitances (a), resistances (b), inductances (c) and resonance frequencies of branches of the lossless circuits (d) of the CF circuit branches (—: branch 1, —: branch 2) and SPIS circuit branches (—: branch 1, —: branch 2). In (d), the tuning rules from Behrens et al. (2003) (- - -) and from Fleming et al. (2003) (- - -) are also plotted.

more robust identification approaches than that proposed in Raze et al. (2020).

Experimental validation of the tuning procedure

The clamped-free piezoelectric beam shown in Figure 10 was used as a host to experimentally validate the

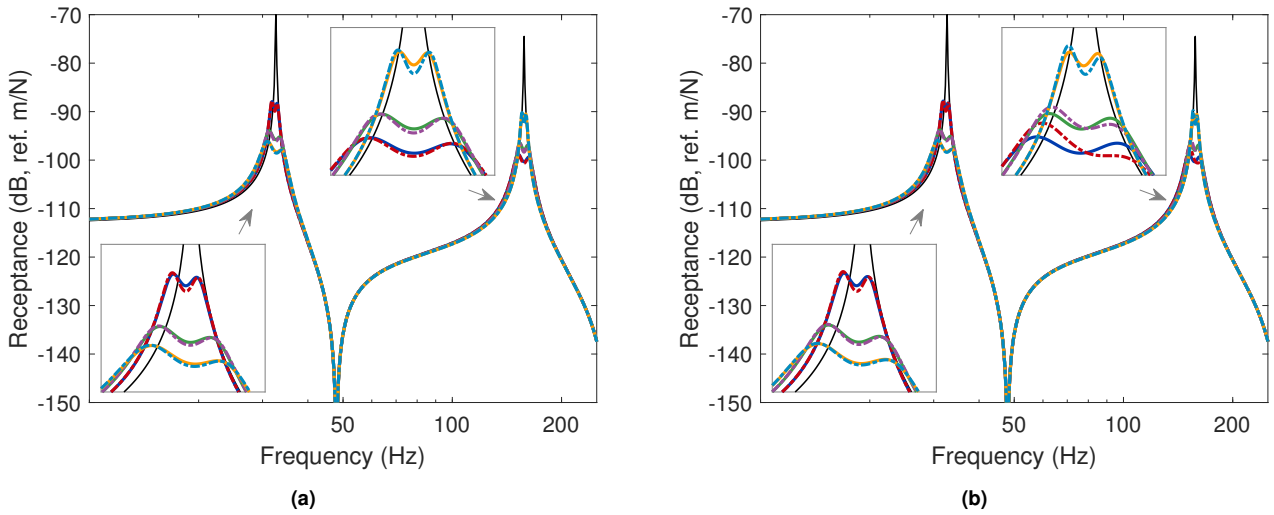

Figure 16. FRF of the beam with open-circuited patches (—), controlled with a CB circuit with series RL shunts (a) and a CB circuit with parallel RL shunts (b), with $r_1 = 0.1$, $r_2 = 0.9$ (— : this work, -·- : Raze et al. (2020)), $r_1 = 0.5$, $r_2 = 0.5$ (— : this work, -·- : Raze et al. (2020)) and $r_1 = 0.9$, $r_2 = 0.1$ (— : this work, -·- : Raze et al. (2020)).

Table 6. Parameters of the CB circuit with series RL shunts.

	R_1	L_1	R_2	L_2	$\tilde{C}_1$	$\tilde{L}_1$
$r_1 = 0.9, r_2 = 0.1$	7.93 kΩ	229.17 H	3.92 kΩ	104.30 H	11.35 nF	2.07 kH
$r_1 = 0.5, r_2 = 0.5$	10.62 kΩ	226.98 H	1.75 kΩ	20.81 H	102.12 nF	232.82 H
$r_1 = 0.1, r_2 = 0.9$	20.14 kΩ	190.89 H	1.28 kΩ	11.62 H	919.11 nF	26.21 H

Table 7. Parameters of the CB circuit with parallel RL shunts.

	R_1	L_1	R_2	L_2	$\tilde{C}_1$	$\tilde{L}_1$
$r_1 = 0.9, r_2 = 0.1$	285.44 kΩ	235.09 H	3 MΩ	104.58 H	11.35 nF	2.12 kH
$r_1 = 0.5, r_2 = 0.5$	212.68 kΩ	235.79 H	338.25 kΩ	21 H	102.12 nF	235.79 H
$r_1 = 0.1, r_2 = 0.9$	95.08 kΩ	236.50 H	668.44 kΩ	11.68 H	919.11 nF	26.28 H

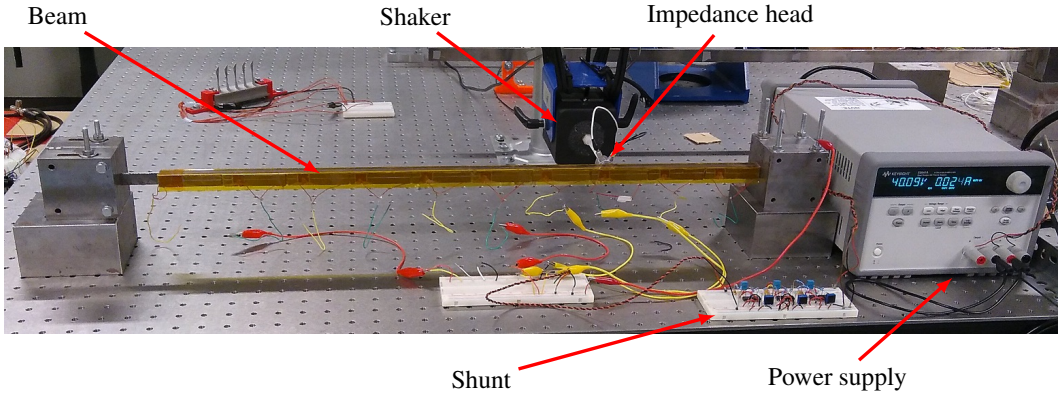

Figure 17. Picture of the experimental setup.

theoretical developments. Figure 17 features a picture of the experimental setup. The beam was excited 20 cm away from the clamped end by an electrodynamic shaker, and an impedance head was used to measure the acceleration of the structure and the force acting on it. The first three bending modes of the beam were targeted for vibration reduction to illustrate the approach with a higher number of modes and to complement the results in Raze et al. (2021). To maximize and balance the electromechanical coupling on these modes, piezoelectric cells 3, 4 and 5 (starting from the clamped end) were connected in parallel, and the other cells were left in open circuit.

System identification

In order to identify the parameters necessary for tuning the shunts, the charge-to-voltage transfer function, i.e., the dynamic elastance of the patches, was measured using an impedance analyzer. A simple nonlinear least-squares fit of the resulting FRF with the law (Raze et al. 2021)

$$\frac{V_p}{q_p} = \frac{1}{C_p^\varepsilon} \frac{\prod_{n=1}^{3} \left(s^2 + 2\xi_n \omega_{oc,n} s + \omega_{sc,n}^2\right)}{\prod_{n=1}^{3} \left(s^2 + 2\xi_n \omega_{oc,n} s + \omega_{oc,n}^2\right)} \tag{92}$$

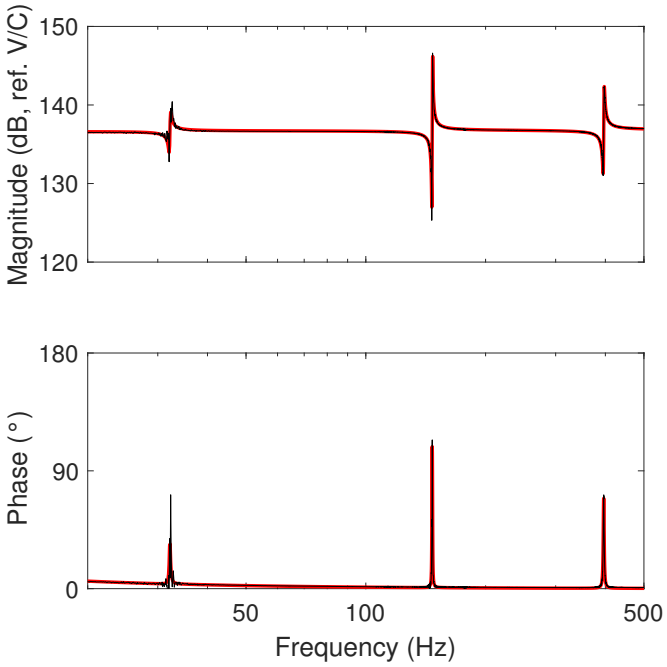

Figure 18. Bode plot of the dynamic elastance: experimental measurements (—) and fitted model (—).

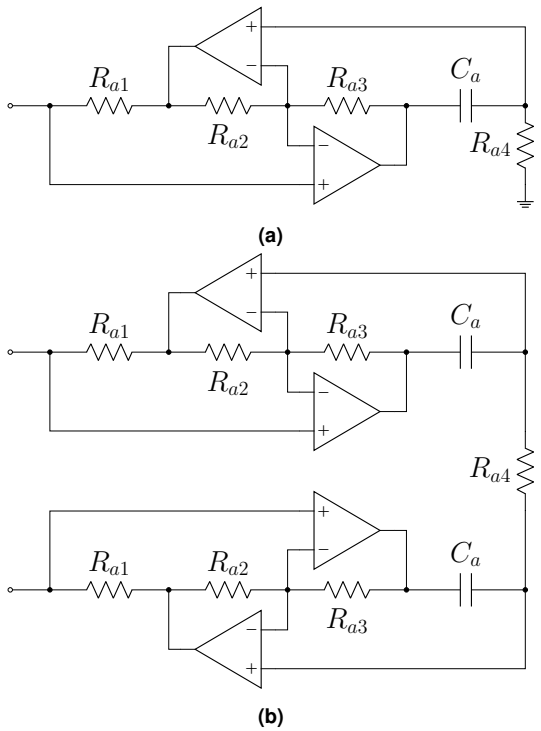

Figure 19. Antoniou's virtual inductor: grounded (a) and floating (b) versions.

(with ξ_n the modal damping ratios) was performed. Since the short- and open-circuit resonance frequencies ($\omega_{sc,n}$ and $\omega_{oc,n}$) of the first three modes correspond to zeros and poles of the dynamic elastance, they were initially determined by the trough and peak frequencies of the measured FRF, respectively. The piezoelectric capacitance at constant strain was estimated by the value of the FRF at high frequency. The impedance analyzer had a small parallel conductance g which was incorporated in the model by

$$sZ_m(s) = \frac{\dfrac{V_p}{q_p}}{1 + g\dfrac{V_p}{sq_p}}, \tag{93}$$

where sZ_m models the measured elastance (Z_m being the measured impedance). The parameters $\omega_{sc,n}$, $\omega_{oc,n}$, ξ_n, C_p^ε and g were then optimized to fit the model given by Equations (92) and (93) to the experimental measurements using the MATLAB function `lsqnonlin`. Figure 18 features a Bode plot of the experimental elastance and its fit, and the extracted parameters are reported in Table 8. In addition, modal damping of approximately 0.2% was identified on all three modes.

Shunts realization

The shunts were realized using passive capacitors and resistors, but the inductances values were too large to allow for finding off-the-shelf components. To emulate these inductors, Antoniou's virtual inductors (schematically depicted in Figure 19) were used (Moheimani and Fleming 2006). The implemented inductance is related to the electrical parameters of this circuit by

$$L = \frac{C_a R_{a1} R_{a3} R_{a4}}{R_{a2}}. \tag{94}$$

In all inductors, the value of R_{a4} was adjusted in function of the other parameters to provide the desired inductance. The other parameters used in this study were $R_{a1} = R_{a2} = R_{a3} = 10$ kΩ and $C_a = 1$ μF, and the operational amplifiers were OPA 445 from Texas Instruments (TI 2008).

Figures 20a and 20b feature a picture of CF and SPIS shunts, respectively. These circuits can readily be transformed into Hollkamp's and SFCF shunts by short-circuiting and open-circuiting one of the capacitors, respectively. We note that with the SPIS/SFCF shunts, two of the virtual inductors are floating (which requires four operational amplifiers per inductor). It was not sought to validate experimentally the developments on the CB shunts since they are close to those obtained by Raze et al. (2020) and those results were already validated therein.

Beam with shunted patches

Figures 21a and 21b present the FRF of the beam when the patches are shunted with Hollkamp's and SFCF shunts, respectively. For the SFCF shunt, the case $r_1 = r_3 = 0.25$ and $r_2 = 0.5$ required a negative resistance, which was not implemented to avoid any risk of instability; the concerned resistor was merely replaced by an open circuit. It should nonetheless be pointed out that all electrical modes are damped by the other resistors. The different curves represent cases where control emphasis is placed on a specific mode. A reduction of 10 to 20 dB can be observed with respect to the open-circuit case, depending on which mode is considered and emphasized, proving the effectiveness of the proposed approach. A qualitative agreement is also obtained in terms of the interpretation of the residues: when emphasis is placed on a mode, the reduction is greater compared to the case where another mode is emphasized. The circuits are most often slightly overdamped, which is manifested by the

Table 8. Identified parameters of the experimental setup, with $\omega_{sc,n} = 2\pi f_{sc,n}$ and $\omega_{oc,n} = 2\pi f_{oc,n}$.

$f_{\mathrm{sc},1}$	$f_{\mathrm{oc},1}$	$f_{\mathrm{sc},2}$	$f_{\mathrm{oc},2}$	$f_{\mathrm{sc},3}$	$f_{\mathrm{oc},3}$	C_p^{ε}
32.13 Hz	32.22 Hz	146.59 Hz	147.15 Hz	395.45 Hz	396.94 Hz	143.89 nF

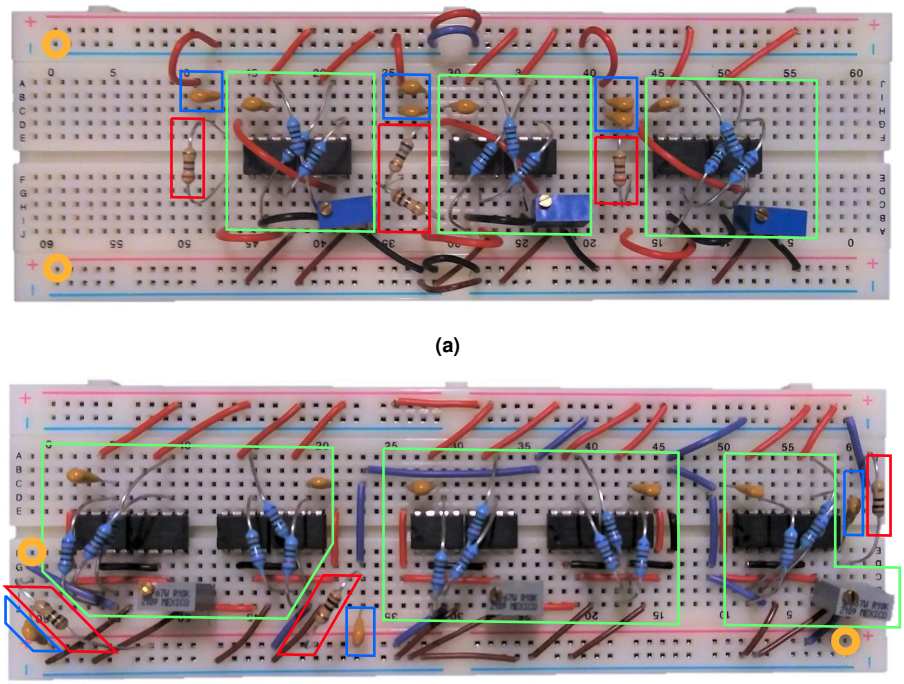

(a)

(b)

Figure 20. Picture of Hollkamp's/CF shunt (a) and the SFCF/SPIS shunt (b) (□: capacitor, □: resistor, □: virtual inductor, ○: connection to the piezoelectric patches).

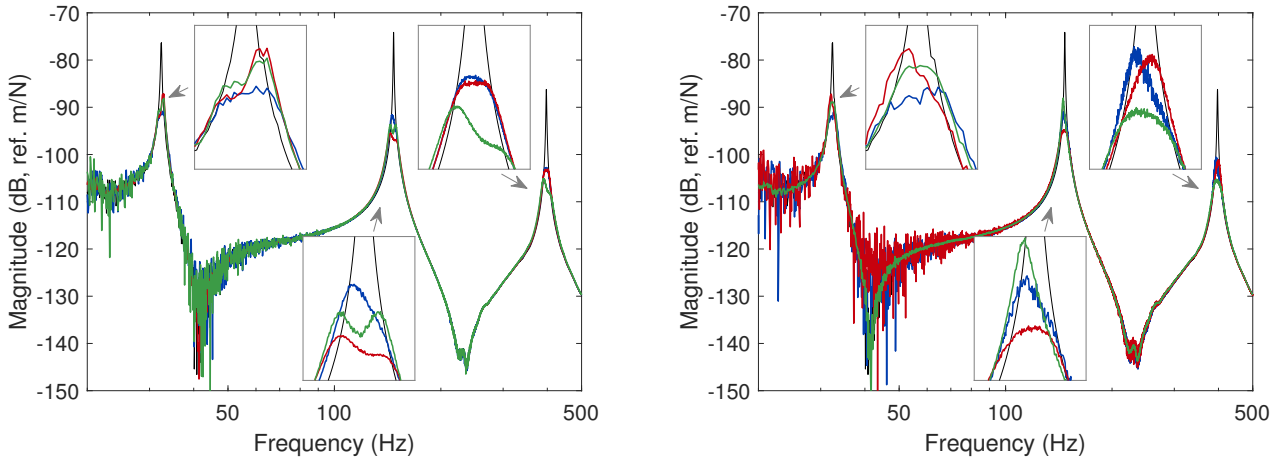

(a) **(b)**

Figure 21. Experimental FRFs of the beam with open-circuited patches (—) and shunted with Hollkamp's (a) and SFCF (b) shunts: $(r_1, r_2, r_3) = (0.5, 0.25, 0.25)$ (—), $(r_1, r_2, r_3) = (0.25, 0.5, 0.25)$ (—) and $(r_1, r_2, r_3) = (0.25, 0.25, 0.5)$ (—).

flat appearance of the double peaks. This effect is more pronounced with the SFCF shunt. Nevertheless, identical sets of residues yield nearly identical vibration reduction performance with both circuits.

Figures 22a and 22b display the FRF of the beam when the patches are shunted with CF and SPIS shunts, respectively. In this case, the residue r_0 which is not associated with any mode is varied. In general, the larger this residue, the smaller the vibration reduction on the modes, in accordance with the numerical analysis. Once again, it can be observed that the circuits are slightly overdamped, and this effect is more pronounced on the SPIS shunt.

The reason for the excessive electrical damping may be attributed to parasitic damping coming from uncontrolled Ohmic losses and capacitor losses. The latter is more prominent for circuits with parallel RL shunts because they require higher capacitance values, and the capacitors needed for such high values are typically coming with relatively high dissipation factors. The imbalance in the peaks may be attributed to the measurement uncertainty

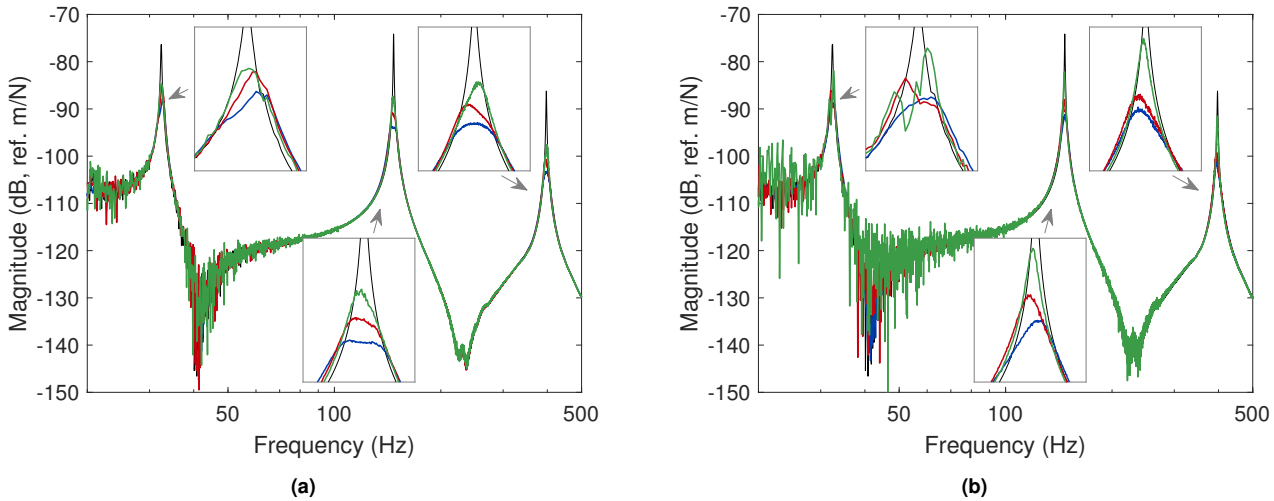

Figure 22. Experimental FRFs of the beam with open-circuited patches (—) and shunted with CF (a) and SPIS (b) shunts: $(r_0, r_1, r_2, r_3) = (0.1, 0.3, 0.3, 0.3)$ (—), $(r_0, r_1, r_2, r_3) = (0.5, 0.16, 0.16, 0.16)$ (—) and $(r_0, r_1, r_2, r_3) = (0.7, 0.1, 0.1, 0.1)$ (—).

on the electrical parameters, especially the capacitances. It should be noted that these two effects can be countered by changing the resistances in the circuits (including R_{a4} to adjust the inductances). Such a fine tuning was not pursued in this work, as significant vibration reduction was already observable, signaling that the electrical resonance frequencies and damping ratios were close to being optimal, and thereby validating the proposed tuning approach. Finally, it should also be reported that all tested circuits exhibited nonlinear behavior, increasing their damping while subjected to higher voltages. This trend is not reported here, but is coherent with the presence of capacitor losses.

Conclusion

This work exploited a recently-proposed specification procedure for multimodal piezoelectric damping to design shunts of known topologies. By relating the ideal Norton's admittance and Thévenin's impedance to those of the considered circuits, it was possible to tune their electrical parameters. Performance in terms of effective coupling (hence in terms of vibration reduction) can be chosen through the values of the residues, but must be traded-off between the modes. The tuning procedure was numerically verified and experimentally validated using a piezoelectric beam. It was demonstrated to provide effective multimodal vibration damping for piezoelectric structures

From the theoretical, numerical and experimental developments made in this work, the following conclusions can be drawn on multimodal shunts:

1. Hollkamp's and the SFCF shunts are the simplest topologies offering optimal multimodal vibration damping, but are not suited for control emphasis on higher-frequency and lower-frequency modes, respectively.
2. The CF and SPIS shunts exhibit at best the same performance as Hollkamp's and the SFCF shunts, respectively, when $r_0 \to 0$. For high values of r_0, they tend to an open circuit and short circuit, respectively, and performance thus degrades.
3. The CB shunt also exhibits optimal performance for a passive circuit, and benefits from the advantage of a relative independence between its different stages. This comes at the expense of a more complex topology with more electrical elements.
4. Besides the CF and SPIS with high r_0, all passive multimodal shunts considered in this work exhibit similar performance in terms of vibration reduction.

This work showed that Hollkamp's, the SFCF and the CB shunts are topologies that theoretically allow for optimal vibration mitigation with multi-resonant shunts. Yet, further investigation of various topologies may still prove useful to find circuits with, e.g., realizable electrical parameters, or to consider non-necessarily resonant control in the same lines as Dal Bo et al. (2022).

An interesting extension of this work could be the fully passive realization of the considered circuits using tailor-made inductors. The problem of designing multiple circuits shunting multiple transducers for improved control performance could also be tackled.

Acknowledgements

The authors would like to acknowledge the financial support of the SPW (WALInnov grant 1610122).

Appendix

Sherman-Morrison formula

The Sherman-Morrison formula allows for the computation of the inverse of a rank-one updated matrix from the inverse of the non-updated matrix $\mathbf{A}$ (Sherman and Morrison 1950), provided it is regular. It is given by

$$\left(\mathbf{A} + \mathbf{u}\mathbf{v}^T\right)^{-1} = \mathbf{A}^{-1} - \frac{1}{1 + \mathbf{v}^T\mathbf{A}^{-1}\mathbf{u}}\mathbf{A}^{-1}\mathbf{u}\mathbf{v}^T\mathbf{A}^{-1}, \tag{95}$$

where $\mathbf{u}$ and $\mathbf{v}$ are vectors of length equal to that of $\mathbf{A}$.

References

Agneni A, Del Sorbo M, Mastroddi F and Polli GM (2006) Multi-modal damping by shunted piezo-patches:

Possible aeroelastic applications. *International Journal of Applied Electromagnetics and Mechanics* 24(1-2): 1–24. DOI:10.3233/JAE-2006-709. URL https://www.medra.org/servlet/aliasResolver?alias=iospress&doi=10.3233/JAE-2006-709.

Alexander CK and Sadiku MNO (2000) *Fundamentals of Electric Circuits*. Cambridge: McGraw-Hill Education. ISBN 0073380571.

Behrens S, Moheimani S and Fleming A (2003) Multiple mode current flowing passive piezoelectric shunt controller. *Journal of Sound and Vibration* 266(5): 929–942. DOI:10.1016/S0022-460X(02)01380-9. URL https://linkinghub.elsevier.com/retrieve/pii/S0022460X02013809.

Berardengo M, Manzoni S and Conti AM (2017) Multi-mode passive piezoelectric shunt damping by means of matrix inequalities. *Journal of Sound and Vibration* 405: 287–305. DOI:10.1016/j.jsv.2017.06.002. URL http://dx.doi.org/10.1016/j.jsv.2017.06.002.

Berardengo M, Manzoni S, Vanali M and Bonsignori R (2021) Enhancement of the broadband vibration attenuation of a resistive piezoelectric shunt. *Journal of Intelligent Material Systems and Structures* : 1045389X20988090DOI: 10.1177/1045389X20988090. URL https://doi.org/10.1177/1045389X20988090.

Berardengo M, Thomas O, Giraud-Audine C and Manzoni S (2016) Improved resistive shunt by means of negative capacitance: new circuit, performances and multi-mode control. *Smart Materials and Structures* 25(7): 075033. DOI:10.1088/0964-1726/25/7/075033. URL https://iopscience.iop.org/article/10.1088/0964-1726/25/7/075033.

Chen WK (2018) *Passive, Active, and Digital Filters*. CRC Press. ISBN 9781315219141. DOI:10.1201/9781315219141. URL https://www.taylorfrancis.com/books/9781420058864.

Cigada A, Manzoni S, Redaelli M and Vanali M (2012) Optimization of the current flowing technique aimed at semi-passive multi-modal vibration reduction. *Journal of Vibration and Control* 18(2): 298–312. DOI:10.1177/1077546311407537. URL http://journals.sagepub.com/doi/10.1177/1077546311407537.

Dal Bo L, He H, Gardonio P, Li Y and Jiang JZ (2022) Design tool for elementary shunts connected to piezoelectric patches set to control multi-resonant flexural vibrations. *Journal of Sound and Vibration* 520(October): 116554. DOI:10.1016/j.jsv.2021.116554. URL https://linkinghub.elsevier.com/retrieve/pii/S0022460X21005757.

Darleux R, Lossouarn B and Deü Jf (2020) Broadband vibration damping of non-periodic plates by piezoelectric coupling to their electrical analogues. *Smart Materials and Structures* 29(5): 054001. DOI:10.1088/1361-665X/ab7948. URL https://iopscience.iop.org/article/10.1088/1361-665X/ab7948.

Edberg DL, Bicos AS and Fechter JS (1991) On piezoelectric energy conversion for electronic passive damping enhancement. In: *Proceedings of Damping*. pp. 717–724.

Fleming A, Behrens S and Reza Moheimani S (2002) Optimization and implementation of multimode piezoelectric shunt damping systems. *IEEE/ASME Transactions on Mechatronics* 7(1): 87–94. DOI:10.1109/3516.990891. URL http://ieeexplore.ieee.org/document/990891/.

Fleming AJ, Behrens S and Moheimani SOR (2003) Reducing the inductance requirements of piezoelectric shunt damping systems. *Smart Materials and Structures* 12(1): 57–64. DOI:10.1088/0964-1726/12/1/307. URL http://stacks.iop.org/0964-1726/12/i=1/a=307?key=crossref.39ab51d3ef8ca1b6552bf22dd04b4ff3.

Franklin GF, Powell JD and Emami-Naeini A (2015) *Feedback Control of Dynamic Systems*. Pearson London. ISBN 978-0-13-468571-7.

Gardonio P, Zientek M and Dal Bo L (2019) Panel with self-tuning shunted piezoelectric patches for broadband flexural vibration control. *Mechanical Systems and Signal Processing* 134: 106299. DOI:10.1016/j.ymssp.2019.106299. URL https://linkinghub.elsevier.com/retrieve/pii/S0888327019305205.

Goldstein AL (2011) Self-Tuning Multimodal Piezoelectric Shunt Damping. *Journal of the Brazilian Society of Mechanical Sciences and Engineering* 33(4): 428–436. DOI:10.1590/S1678-58782011000400006. URL http://www.scielo.br/scielo.php?script=sci_arttext&pid=S1678-58782011000400006&lng=en&nrm=iso&tlng=en.

Hagood N and von Flotow A (1991) Damping of structural vibrations with piezoelectric materials and passive electrical networks. *Journal of Sound and Vibration* 146(2): 243–268. DOI:10.1016/0022-460X(91)90762-9. URL https://linkinghub.elsevier.com/retrieve/pii/0022460X91907629.

Hollkamp JJ (1994) Multimodal Passive Vibration Suppression with Piezoelectric Materials and Resonant Shunts. *Journal of Intelligent Material Systems and Structures* 5(1): 49–57. DOI:10.1177/1045389X9400500106. URL http://journals.sagepub.com/doi/10.1177/1045389X9400500106.

Lossouarn B, Deü JF and Kerschen G (2018) A fully passive nonlinear piezoelectric vibration absorber. *Philosophical Transactions of the Royal Society A: Mathematical, Physical and Engineering Sciences* 376(2127): 20170142. DOI:10.1098/rsta.2017.0142. URL http://rsta.royalsocietypublishing.org/lookup/doi/10.1098/rsta.2017.0142.

Moheimani SOR and Fleming AJ (2006) *Piezoelectric Transducers for Vibration Control and Damping*. Advances in Industrial Control. London: Springer-Verlag. ISBN 1-84628-331-0. DOI: 10.1007/1-84628-332-9. URL http://link.springer.com/10.1007/1-84628-332-9.

Raze G (2021) *Piezoelectric Digital Vibration Absorbers for Multimodal Vibration Mitigation of Complex Mechanical Structures*. PhD Thesis, University of Liège, Liège, Belgium. URL http://hdl.handle.net/2268/256608.

Raze G, Dietrich J and Kerschen G (2021) Passive control of multiple structural resonances with piezoelectric vibration absorbers. *Journal of Sound and Vibration* 515(August): 116490. DOI:10.1016/j.jsv.2021.116490. URL https://linkinghub.elsevier.com/retrieve/pii/S0022460X21005253.

Raze G, Paknejad A, Zhao G, Collette C and Kerschen G (2020) Multimodal vibration damping using a simplified

current blocking shunt circuit. *Journal of Intelligent Material Systems and Structures* 31(14): 1731–1747. DOI: 10.1177/1045389X20930103. URL http://journals.sagepub.com/doi/10.1177/1045389X20930103.

Sherman J and Morrison WJ (1950) Adjustment of an Inverse Matrix Corresponding to a Change in One Element of a Given Matrix. *The Annals of Mathematical Statistics* 21(1): 124–127. DOI:10.1214/aoms/1177729893. URL http://projecteuclid.org/euclid.aoms/1177729893.

Thomas O, Deü JF and Ducarne J (2009) Vibrations of an elastic structure with shunted piezoelectric patches: efficient finite element formulation and electromechanical coupling coefficients. *International Journal for Numerical Methods in Engineering* 80(2): 235–268. DOI:10.1002/nme.2632. URL http://doi.wiley.com/10.1002/nme.2632.

Thomas O, Ducarne J and Deü JF (2012) Performance of piezoelectric shunts for vibration reduction. *Smart Materials and Structures* 21(1): 015008. DOI: 10.1088/0964-1726/21/1/015008. URL http://stacks.iop.org/0964-1726/21/i=1/a=015008?key=crossref.6d8696aab65a8889d18c15289623f766.

TI (2008) High Voltage FET-Input OPERATIONAL AMPLIFIER. URL https://www.ti.com/product/OPA445.

Toftekær JF and Høgsberg J (2020) Multi-mode piezoelectric shunt damping with residual mode correction by evaluation of modal charge and voltage. *Journal of Intelligent Material Systems and Structures* 31(4): 570–586. DOI: 10.1177/1045389X19891646. URL http://journals.sagepub.com/doi/10.1177/1045389X19891646.

Wu SY (1996) Piezoelectric shunts with a parallel R-L circuit for structural damping and vibration control. In: Johnson CD (ed.) *Spie*, volume 2720. ISBN 0819420956, pp. 259–269. DOI:10.1117/12.239093. URL http://proceedings.spiedigitallibrary.org/proceeding.aspx?articleid=1017503.

Wu SY (1998) Method for multiple-mode shunt damping of structural vibration using a single PZT transducer. In: Davis LP (ed.) *Smart structures and materials 1998: passive damping and isolation*, volume 3327. pp. 159–168. DOI:10.1117/12.310680. URL http://proceedings.spiedigitallibrary.org/proceeding.aspx?articleid=940157.